Available online at www.sciencedirect.com

ScienceDirect

Underground Space 12 (2023) 44–64

www.keaipublishing.com/undsp

Numerical prediction of ground vibrations induced by LPG boiling liquid expansion vapour explosion (BLEVE) inside a road tunnel

Ruishan Cheng [a], Wensu Chen [a,*], Hong Hao [b,a,*], Jingde Li [a]

[a] *Center for Infrastructural Monitoring and Protection, School of Civil and Mechanical Engineering, Curtin University, Bentley 6102, Australia*
[b] *Earthquake Engineering Research & Test Center, Guangzhou University, Guangzhou 510006, China*

Received 15 August 2022; received in revised form 2 February 2023; accepted 7 February 2023
Available online 24 May 2023

Abstract

Accidental boiling liquid expansion vapour explosions (BLEVEs) caused by the bursting of liquified petroleum gas (LPG) tank inside a tunnel can induce vibrations of its surrounding geological media and threaten the stability of adjacent tunnels and structures. Therefore, it is essential to understand the characteristics of vibrations induced by LPG BLEVEs inside the tunnel for the safety design of its adjacent structures. Owing to the difficulty in effectively predicting the LPG BLEVE loads, the current practice usually employs equivalent methods, e.g., the TNT-equivalency method, in LPG BLEVE load predictions for structural response analysis, which may lead to inaccurate response predictions. This study compares ground vibrations induced by a BLEVE inside an arched road tunnel with those induced by its equivalent TNT explosion via high-fidelity numerical simulations. The results demonstrate that the frequency of BLEVE-induced vibrations is lower than that induced by the TNT explosion at the same scaled distance. The intensity of LPG BLEVE-induced vibrations at relatively small-scaled distances is lower than that of TNT explosion-induced vibrations at the same scaled distance, but becomes higher after a certain scaled distance because of the relatively low attenuation rate. In addition, parametric analysis is conducted to evaluate the effects of various factors on the characteristics of LPG BLEVE-induced ground vibrations. It is found that the surrounding rock type, the rock porosity, and the cover depth of the tunnel have more significant influences than the concrete grade of the tunnel lining. The recommendation for the tunnel design is also given based on the intensity and frequency characteristics of BLEVE-induced vibrations.

Keywords: Tunnel; BLEVE; TNT explosion; Vibration intensity; Vibration frequency

1 Introduction

As essential parts of modern traffic flow, road tunnels have been widely constructed in urban and rural areas (Cheng et al., 2021; Goel et al., 2021). Many of them are built side-by-side (e.g., two tubes with a certain spacing) to separate the traffic flow, as well as to save urban space and overcome narrow terrain restrictions in mountain areas (Vinod & Khabbaz, 2019). During operation, road tunnels may undergo (1) internal high explosive (HE) explosions as a result of terrorist activities or explosive transportation accidents, and (2) internal boiling liquid expansion vapour explosions (BLEVEs) as a result of the transported gas or fuel tank failure. These accidental explosions inside one tunnel can induce vibrations of its surrounding rock mass or soil mass and endanger the neighbouring tunnels (Li et al., 2013). In order to understand the response of a tunnel subjected to vibrations induced by explosions in a neighbouring tunnel, provide effective protection or mitigation measures for the adjacent tunnel, and design a safe separation distance between neighbouring tunnels, this study investigates the vibration

* Corresponding author.
E-mail addresses: wensu.chen@curtin.edu.au (W. Chen), hong.hao@curtin.edu.au (H. Hao).

https://doi.org/10.1016/j.undsp.2023.02.007

characteristics of geological media induced by different types of explosions inside a road tunnel.

Many empirical formulae have been developed in existing studies to evaluate and predict the vibration characteristics (e.g., intensity and frequency) induced by open-pit and underground blasting or explosions (Kan et al., 2022; Paneiro & Rafael, 2021; Yan et al., 2020). The typical one based on the site condition coefficients and the scaled distance (i.e., standoff distance L divided by the cube root of charge weight W), is widely used to evaluate the vibrations of geological media induced by accidental tunnel explosions (Hao et al., 2001; Wu & Hao, 2005; Wu, Hao, et al., 2003, Wu et al., 2003; Zhou, 2011; Zhu et al., 2018). For instance, Wu and Hao (2005) developed empirical formulae based on the scaled distance and site condition coefficients to predict the attenuation of the intensity and principal frequency of vibrations inside granite rock mass and on the ground surface induced by TNT explosions in an underground rock chamber. The results indicated that the attenuation characteristics of vibrations in rock mass differed from those on the ground surface due to the stress wave reflections at the ground surface. Hao et al. (2001) also performed field blasting tests and studied the characteristics of the ground vibrations induced by TNT explosions inside a tunnel-like underground chamber in the jointed rock mass. The results revealed that the spatial variation of blast-induced ground vibrations was more significant than that of seismic motions due to the higher frequency contents of blast-induced vibrations. The developed empirical formulae from those studies can approximately predict the vibrations induced by accidental tunnel explosions by considering the specific site conditions and explosion conditions.

In addition, many factors influencing tunnel explosion-induced ground vibrations have been investigated to improve the prediction accuracy of blasting vibrations. Hao and Wu (2001) investigated the effects of the loading density (explosive weight divided by tunnel volume), tunnel geometry, and explosive location and distribution on the characteristics of blast-induced vibrations. The results revealed that increasing the loading density increased the vibration intensity but decreased the principal frequency of vibrations. The attenuation of blasting vibrations was also significantly influenced by the tunnel shape and explosive distribution pattern, while the vibration intensity was barely affected by the variation of tunnel volume. Wu et al. (2004) numerically analyzed the influence of charge weight on blasting vibration characteristics. The results indicated that increasing the charge weight had a negligible influence on the vibration intensity but decreased the principal frequency of vibrations at the same scaled distances with a given loading density. Tiwari et al. (2016) investigated the attenuation characteristics of vibrations induced by a TNT explosion in a circular tunnel with three different weathered quartzite rocks. The results showed that a higher weathered level of rock mass contributed to a more significant attenuation of blasting vibration intensities. Zhu et al. (2018) investigated the effects of joint properties including joint stiffness, joint dip angle, crossing angle and joint spacing on the blasting vibration intensity. It was found that the intensity of blasting vibrations increased with the decreasing joint dip angle and the increasing joint stiffness, joint spacing, and joint crossing angle. Tiwari et al. (2017) also analyzed the effects of soil properties on the attenuation characteristics of blasting vibrations induced by a TNT explosion in a circular tunnel. The results showed that the attenuation of blasting vibration intensity is more significant in soil mass with a higher internal friction angle. It can be concluded that explosion conditions and site conditions including geology properties and tunnel configurations have great influences on the vibration characteristics induced by accidental explosions in tunnels.

The aforementioned studies focused on investigating the characteristics and influence factors of vibrations induced by HE explosions inside tunnels or tunnel-like chambers. Very limited studies evaluated the vibration characteristics induced by BLEVEs inside tunnels. Because of the lack of studies of BLEVE-induced vibrations, in practice, the results obtained from TNT explosions are normally used to assess the risk of accidental explosions caused by accidents of transportation of liquefied gas tankers inside road tunnels. No study compares the vibrations induced by HE explosions and BLEVEs. Based on the fact that BLEVE-induced blast waves have longer duration, slower rising time, and lower peak pressure than equivalent HE explosion-induced blast waves (Hao et al., 2016), the characteristics of blasting vibrations induced by BLEVEs inside tunnels would be different from those induced by the equivalent HE explosions. Therefore, an investigation on vibration characteristics induced by BLEVEs inside tunnels is essential to provide guidance for the safe design and protection of tunnels and adjacent structures against accidental explosions in road tunnels.

In this study, rock vibrations induced by a liquified petroleum gas (LPG) BLEVE inside an arched road tunnel are investigated based on numerical models established in LS-DYNA. The vibration characteristics caused by the LPG BLEVE are compared with the corresponding ones induced by its TNT-equivalence explosion. To comprehensively understand the vibration characteristics induced by BLEVEs inside tunnels, the effects of rock porosities, rock types, tunnel cover depths, and lining concrete grades on LPG BLEVE-induced vibrations are further investigated. The suggestions for the road tunnel design are also provided from the perspective of minimizing the BLEVE-induced vibrations.

2 Numerical model and calibration

In this section, the numerical models of a curved-wall-arched road tunnel subjected to a BLEVE and its TNT-equivalence explosion are respectively established to examine the vibration difference under two explosions. Since LS-DYNA cannot directly simulate the process of

BLEVE, BLEVE loads acting on the road tunnel are generated using computational fluid dynamics software FLACS. Then, the generated BLEVE loads are directly applied to the inner wall of the road tunnel built in LS-DYNA to investigate the response of road tunnel and surrounding media. Therefore, the air domain inside the tunnel is not included in the LS-DYNA model, but it is included in the FLACS model when simulating BLEVE and pressure wave propagation. FLACS is a code to simulate gas explosions and pressure wave propagation, but cannot model dynamic structural responses. Therefore, it is used together with LS-DYNA to calculate tunnel responses. LS-DYNA has the capability of simulating TNT explosions. To obtain TNT explosion loads acting on the inner wall of the road tunnel, the TNT explosive and air domain inside the tunnel are modelled to simulate the whole process of TNT explosion inside tunnel using a popular ALE algorithm in LS-DYNA. The equivalent TNT explosive weight is obtained by transforming the BLEVE energy based on the TNT equivalence method proposed by Prugh (1991). The details are given below.

2.1 Finite element model of the tunnel subjected to BLEVE

Without losing the generality, the Qidaoliang tunnel (Lai et al., 2016) is taken as the example in this study. Figure 1(a) depicts its quarter-axisymmetric numerical model. The model domain of 30 m (length) × 30 m (width) × 60 m (height) is determined by domain convergence tests, which ensures that the reflected waves from the numerical boundary are insignificant to the calculated ground vibrations. Due to the symmetry of the arched tunnel along the cross sections at the explosion centre, e.g., *yz* and *xz* planes at the explosion centre in Fig. 1(a), a quarter

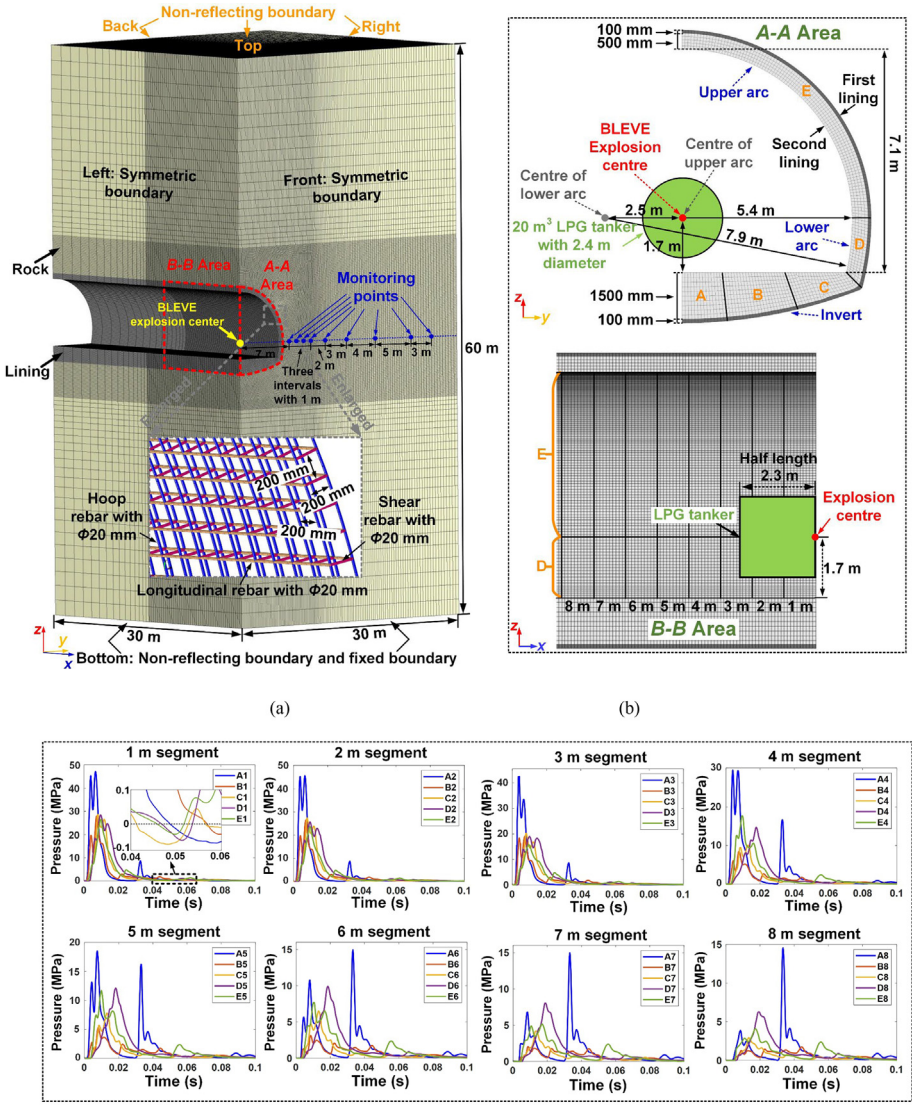

(a) (b)

(c)

Fig. 1. Finite element model of road tunnel and monitoring arrangement under internal BLEVE. (a) Whole numerical model and monitoring arrangement, (b) lining model and BLEVE loading segments, and (c) BLEVE loading time histories.

numerical model is built by assigning the symmetric boundary to the front and left surfaces of the numerical model to save computational cost. The method using the symmetric boundary to reduce the model size of deep ground has been widely utilized and its accuracy for response prediction of deep ground has been validated by many previous studies. The non-reflecting fixed boundary is set to the bottom surface of the numerical model to prevent the numerical model from moving vertically under internal blast loads. The non-reflecting boundary is specified to the model's back, right, and bottom surfaces to minimize the effect of stress wave reflection at the model boundary. In reality, this road tunnel section with a 100 m cover-depth is used for the investigation. However, to reduce the computational efforts, only 30 m cover from the explosion centre (i.e., the centre of the curved-wall-arched tunnel) is modelled. Therefore, the non-reflecting boundary is also assigned to the top surface of the numerical model. A 30 m distance from the explosion centre in the model with a transmitting boundary is sufficient to ensure that the monitored ground vibrations in rock mass are hardly affected by the reflected stress waves from the ground surface. Therefore, the remaining 70 m rock cover above the road tunnel is not included to save computational costs. However, the in-situ stresses of rock mass around the tunnel with 100 m cover depth are calculated and applied to the built model to simulate the stress states of the tunnel with a 100 m cover depth. The empirical equations developed by Li et al. (2016) as well as Brown and Hoek (1978) are used to calculate the in-situ stresses at the 100 m cover-depth. The stress initialization of numerical model of road tunnels, i.e., incorporating the calculated in-situ stresses into the model, is achieved by a quasi-static method (i.e., using first rising and then constant in-situ stress loading curves combined with explicit calculation (Yang et al., 2020). The details have been reported in the authors' previous paper (Cheng et al., 2022b) and thus are not repeated herein. Nine monitoring points at the same level as the explosion centre are arranged inside the rock mass in the explosion centre's cross-section along the width of numerical models to record velocity time histories at the corresponding locations. Horizontal distances of the nine monitoring points from the explosion centre are shown in Fig. 1(a).

The half cross-sectional tunnel is composed of a lower arc (i.e., partial circle) with an inner radius of 7.9 m, an invert with the vertical distance of 1.7 m from the explosion centre, and an upper arc (i.e., a quarter circle) with an inner radius of 5.4 m, as shown in Fig. 1(b). The thickness of second lining of the upper and lower arcs is 500 mm. The thickness of second lining of the invert varies from 500 mm at the corner to 1.5 m at the middle invert. The thickness of first lining of the tunnel is 100 mm. The lining near explosion centre is meshed by using 100 mm solid elements, which are determined via mesh convergence test, i.e., comparing with the tunnel response under different mesh sizes from 50 to 200 mm. To improve computational efficiency, the remaining lining and rock mass are meshed by gradually increasing the sizes of solid elements (e.g., from 100 to 450 mm along the direction of monitoring points) as the distance from the explosion centre increases. The secondary lining of the road tunnel constructed in IV and weaker levels of rock mass needs to be reinforced by steel rebars, for example, as specified in the design standard of road tunnel in China (Ministry of, 2018). Therefore, the composite lining with the reinforced secondary lining is considered as a typical form of lining of the road tunnel surrounded by the rock mass defined above. The arrangements of steel reinforcements in the second lining are shown in Fig. 1(a). Longitudinal and hoop rebars with a 20 mm diameter are designed as two layers with an interval of 200 mm. Adjacent longitudinal rebars or hoop rebars in each layer have the same interval of 200 mm. Shear rebars with a 20 mm diameter are installed between two layers of longitudinal and hoop meshes. The 50 mm size of beam elements determined via mesh convergence tests are used to mesh steel reinforcements in the second lining.

A BLEVE case due to the bursting of a liquified petroleum gas (LPG) tank with 20 m^3 (i.e., the LPG tank with a length of 4.6 m and a diameter of 2.4 m) is considered inside the arched tunnel (see Fig. 1(b)). The centre of the LPG tank is located at the centre of the upper arc of the curved-wall-arched tunnel. In this scenario, the FLACS, a computational fluid dynamic (CFD) code, is used to generate BLEVE loads considering vapour expansion and instantaneous liquid flashing (See Appendix A). It should be noted that the authors have proven the reliability of FLACS in modelling BLEVEs (Li et al., 2022; Li & Hao, 2020), which is not thus repeated herein. These BLEVE loads are then applied to the numerical model's inner tunnel wall in LS-DYNA. The first eight 1-m segments along the length of tunnel are selected as the BLEVE loading segments (See *B-B* Area in Fig. 1(b)). Each segment is further divided into five parts (See *A-A* Area in Fig. 1(b)). Since very minor tunnel-response difference is observed when subjected to uniform and non-uniform BLEVE loads, the BLEVE load is considered to be uniform on each part for simplification. Each part in LS-DYNA is imposed with BLEVE loads (see Fig. 1(c)) obtained at the centre of the corresponding part in FLACS.

Multiple peaks of the BLEVE overpressure near 0.01 s in the overpressure time histories applied to the A segment (i.e., A1–A8) of Fig. 1(c) are due to multiple reflections of BLEVE waves between the tunnel floor and the LPG tank. The local peak overpressure occurred near 0.04 s is due to the reflected BLEVE waves from the tunnel arched wall acting on the tunnel floor. Since the present study focuses on the ground vibration induced by BLEVE loads, the comparison of BLEVE loads in confined and open spaces is not provided in this study.

2.2 Equivalent TNT weight and corresponding model

BLEVE loads are difficult to be directly estimated and often approximated by using empirical methods for struc-

tural design and analysis. One of the most widely used empirical methods for the BLEVE loading prediction is the TNT equivalence method proposed by Prugh (1991) (See Appendix B). This method can transform the energy of the liquid explosive flashing at the moment of tank rupture and the high-pressurized vapour inside the LPG tank into an equivalent TNT weight. Therefore, the TNT equivalence explosion has the same energy release as the BLEVE. To compare the difference of ground vibrations induced by the BLEVE and TNT explosion, a TNT weight (i.e., 1150 kg) equivalent to the BLEVE assumed in Section 2.1 is calculated herein by the TNT equivalence method. The specific calculation process using the TNT equivalence method and the details of parameter acquisition have been reported in the authors' previous paper (Cheng et al., 2022a) and are not repeated herein. Unlike the direct application of BLEVE loading time histories to the inner surface of the tunnel, the TNT-equivalence explosion is simulated by using the keyword *INITIAL_DETONATION in LS-DYNA. TNT explosive with the dimension of 450 mm (length) × 450 mm (width) × 900 mm (height) is built, as shown in Fig. 2. The centre of TNT explosive is 1.7 m from the floor, i.e., at the same location as the BLEVE centre. The air domain is also established to fill the space between the explosive and tunnel lining. The air shares common nodes at its interfaces with the explosives and lining. The front and left surfaces of tunnel and air domain inside the tunnel are assigned symmetric boundaries due to the symmetry of the tunnel and air inside the tunnel along the *yz* and *xz* planes at the explosion centre. Their back surface is assigned with non-reflecting boundary to minimize the reflection of stress waves at the back surface. No boundary condition is assigned to the right faces of the air and tunnel structure since common nodes are shared at the corresponding locations.

The explosive and air are modelled by the Arbitrary Lagrangian-Eulerian (ALE) process. The element size of approximately 100 mm is determined to mesh air and explosive by mesh convergence tests considering accuracy and efficiency. In this study, material models and equations of state (EOS) for air and explosive are referred to Wei et al. (2009) and are tabulated in Table 1.

Figure 3 shows pressure time histories caused by the TNT explosion and LPG BLEVE acting on the inner wall of the arch tunnel lining along the longitudinal direction of the tunnel. It can be found that TNT-equivalence explosion waves have higher peak overpressures, less impulses, and shorter durations and rise time than BLEVE-induced waves. The difference between two types of explosion loads is mainly attributed to different explosion mechanisms. A TNT explosion is a chemical reaction and its detonation velocity is very high, while a BLEVE is a physical explosion and its pressure wave velocity is much lower than that of the TNT explosion. Therefore, TNT explosion of the same energy induces higher overpressure, faster pressure rise and

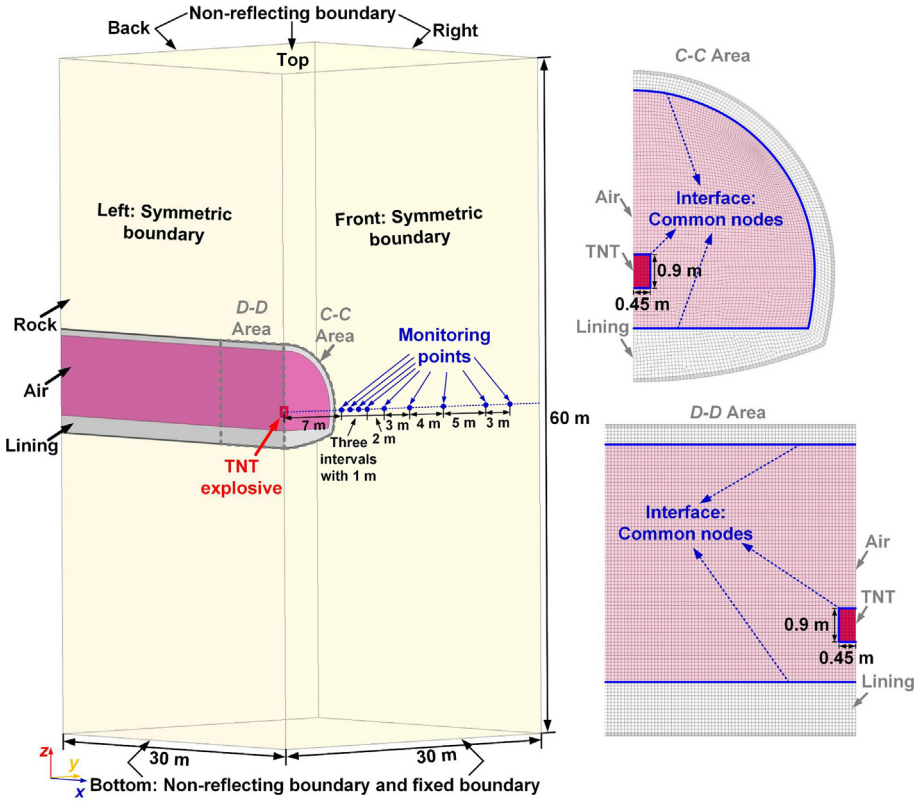

Fig. 2. Numerical model of road tunnel under internal TNT explosion loading.

Table 1
Parameters (Wei et al., 2009) and properties of explosive and air.

Component	Material model and EOS	Parameter	Value
TNT explosive	*MAT_HIGH_EXPLOSIVE_BURN	Chapman-Jouget pressure (GPa)	21
		Detonation velocity (m/s)	6930
	*EOS_JWL	Constant R_1	4.15
	$P = A(1-\frac{\omega}{R_1 V})e^{-R_1 V} + B(1-\frac{\omega}{R_2 V})e^{-R_2 V} + \frac{\omega E}{V}$	Constant B (GPa)	3.747
		Constant A (GPa)	373.8
		Constant R_2	0.9
		Initial internal energy E_0 (J/m^3)	6×10^9
		Constant ω	0.35
Air	*MAT_NULL	Density (kg/m^3)	1.255
	*EOS_LINEAR_POLYNOMIAL	Initial internal energy (J/m^3)	2.5×10^5
	$P_1 = C_0 + C_1\mu + C_2\mu^2 + C_3\mu^3 + (C_4 + C_5\mu + C_6\mu^2)E_r$	Constants C_4, C_5	0.4
		Constants C_0, C_1, C_2, C_3, C_6	0

Note: V, P and μ are the relative volume, hydrostatic pressure, and compression parameter, respectively. E and E_r are the internal energy of explosive and air per unit volume, respectively.

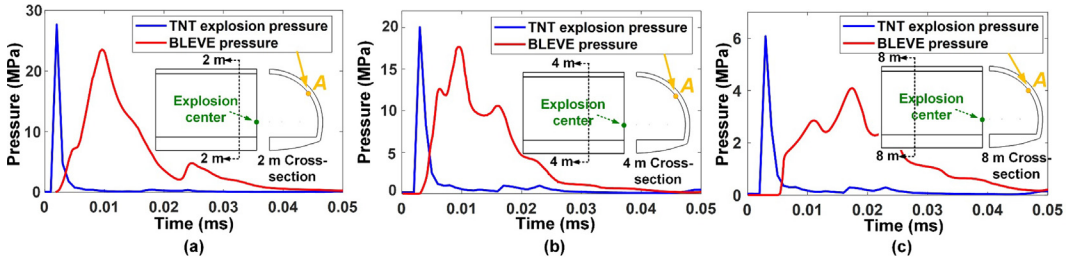

Fig. 3. Comparison of BLEVE and TNT explosion pressures at point A in (a) section segment at 2 m, (b) section segment at 4 m, and (c) section segment at 8 m.

shorter loading duration than BLEVE pressure wave. In addition, the impulse of TNT explosion loads is lower than that of BLEVE loads. It is because with the same energy release, the TNT explosion with high detonation velocity generates blast waves with higher wave velocity and thus lower impulse (i.e., the smaller integration of force over time). The loading difference between the LPG BLEVE and TNT explosion inevitably induces different ground vibrations, which are discussed in detail in the subsequent sections.

2.3 Material models of lining and rock mass

The behaviours of lining concrete, steel reinforcements, and surrounding rock mass of the tunnel are respectively simulated by *MAT_CONCRETE_DAMAGE_REL3, *MAT_PIECEWISE_LINEAR_PLASTICITY, and *MAT_RHT in LS-DYNA. The compressive strength, Poisson's ratio, and density of concrete are 25 MPa, 0.2, and 2300 kg/m^3, respectively. The yield stress, Poisson's ratio, density, and Young's modulus are 300 MPa, 0.3, 7850 kg/m^3, and 210 GPa, respectively. In addition, the strain rate effects, i.e., the dynamic increase factors (DIF) with respect to different strain rates, for steel rebars are modelled by the empirical relations proposed by Malvar (1998), and those for concrete are modelled by Hao and Hao (2014) respectively by using the keyword * DEFINE_CURVE in LS-DYNA. The arched tunnel's surrounding rock mass is sandstone.

The parameters of the *MAT_RHT model for sandstone are listed in Table 2. The basic parameters of sandstone obtained from the Qidaoliang tunnel's field tests can refer to Yang (2006). The parameters significantly influencing the response of rock mass (i.e., A, N, β_c, β_t, P_{el}, A_1, A_2, and A_3 in Table 2) are determined based on the empirical equations given in Liu et al. (2018). The remaining parameters not significantly affecting the rock mass response are obtained from Xie et al. (2017). The performance of rock mass simulated by the Riedel-Hiermaier-Thoma (RHT) model is mainly governed by the basic parameters and those parameters significantly influencing the response of rock mass. The basic parameters are obtained according to the site investigation and field tests conducted by Yang (2006). Although random fluctuations of the parameters significantly influencing the rock response are inevitable, the accuracy of empirical equations used to calculate these parameters has been proved by many studies (Cheng et al., 2022a; Liu et al., 2018; Xie et al., 2017), which represents the mean or most credible values of the rock mass parameters under consideration. In the present study, the accuracy of those parameters determined by empirical equations in predicting the response of rock mass is also calibrated by the test results of an underground chamber subjected to internal explosions (Wu et al., 2003). Therefore, it is concluded that these

Table 2
RHT model parameters for sandstone (Liu et al., 2018; Xie et al., 2017; Yang, 2006).

Type of parameter	Specific parameter	Value	Specific parameter	Value
Strength parameters	Failure surface parameter A	2.7	Failure surface parameter N	0.65
	Lode angle dependence factor Q_0	0.68	Lode angle dependence factor B	0.05
	Compressive yield surface parameter G_c	0.53	Tensile yield surface parameter G_t	0.7
	Volumetric plastic strain fraction in tension P_{tf}	0.001	Erosion plastic strain E_{psf}	2
	Shear modulus reduction factor X_i	0.5	Minimum damaged residual strain E_{pm}	0.015
	Residual surface parameter A_f	0.25	Residual surface parameter N_f	0.62
Basic parameters	Compressive strength (MPa)	41	Relative tensile strength	0.08
	Density (kg/m^3)	2600	Relative shear strength	0.8
	Elastic shear modulus (GPa)	28		
Strain rate parameters	Reference compressive strain rate E_{0c}	3×10^{-5}	Reference tensile strain rate E_{0t}	3×10^{-6}
	Break compressive strain rate E_c	3×10^{25}	Break tensile strain rate E_t	3×10^{25}
	Compressive strain rate dependence exponent β_c	0.028	Tensile strain rate dependence exponent β_t	0.033
Damage parameters	Damage parameter D_1	0.04	Damage parameter D_2	1
EOS parameters	Initial porosity α_0	1.0	Porosity exponent N_p	3
	Crush pressure P_{el} (MPa)	27.33	Compaction pressure P_{co} (GPa)	6
	Gruneisen gammaγ	0	Hugoniot polynomial coefficient A_1 (GPa)	25.36
	Hugoniot polynomial coefficient A_2 (GPa)	37.34	Hugoniot polynomial coefficient A_3 (GPa)	21
	Parameter for polynomial EOS B_0	1.22	Parameter for polynomial EOS B_1	1.22
	Parameter for polynomial EOS T_1 (GPa)	36.22	Parameter for polynomial EOS T_2	0

RHT model parameters listed in Table 2 can give accurate predictions of rock mass responses.

2.4 Model calibration

The model to predict lining responses of road tunnel has been calibrated by the authors in the previous study. To avoid repetition, the calibration of tunnel lining model is not given in this study, and the details of the lining model calibration can refer to Cheng et al. (2022a). In addition, the present study focuses on the ground vibration of rock mass induced by BLEVE and TNT equivalence explosion inside the tunnel. Peak vibration velocities and frequencies obtained from velocity time histories in rock mass are utilized to analyze and evaluate the ground vibration effects. Therefore, velocity time histories of ground vibrations in rock mass and their frequency spectra are calculated and compared with the test results of rock mass vibrations induced by an explosion inside an underground chamber (Wu et al., 2003). The calibration results show that the simulated velocity time histories and frequency spectra agree well with the test data. The details are given below.

2.4.1 Description of the test and simulation

In the field test, an underground rock chamber of 3.9 m (H) × 8.8 m (W) × 33 m (L) with a cover depth of 80 m was subjected to an internal explosion of 10 tons of TNT (Zhou et al., 2002), as shown in Fig. 4(a). The test is used for the calibration of the numerical model. The 10 tons of TNT explosive are evenly divided into 10 bundles. The arrangements of 10 charges are shown in Fig. 4(a). One pressure gauge is put at 0.9 m above the chamber floor to measure explosion pressure. The chamber was closed during the explosion test by closing the blast doors installed between the chamber and its access tunnel. The details can refer to Wu et al. (2003). To measure the rock mass's velocity response, three speedometers with the same height of 1.5 m above the chamber floor are installed at 18, 10, and 6 m from the right chamber wall.

A quarter symmetric numerical model including air, explosive, and rock chamber is built based on the above test setup. The overall model domain is 30 m (L) × 36 m (H) × 25 m (W), and the dimension of the rock chamber is 16.5 m (L) × 3.9 m (H) × 4.4 m (W), as shown in Fig. 4(b). Based on mesh convergence analysis, 100 mm is determined as the mesh size of the rock mass around the chamber. To improve computational efficiency, the rock mass's mesh size is gradually raised as the distance from the chamber increases. In addition, explosives and air inside the chamber are meshed by 100 mm solid elements based on mesh convergence tests. The numerical model's front and left surfaces are assigned with symmetric boundary. The numerical model's bottom top, back, and right surfaces are specified with non-reflection boundaries. To prevent the numerical model from moving vertically under internal blast loads, the model's bottom surface is assigned a fixed boundary. Common nodes at the interfaces of explosive and air are shared. Basic mechanical parameters of *MAT_RHT are obtained according to Wu et al. (2003) and other parameters refer to Table 2. Parameters and EOS of air and explosive refer to Table 1. The in-situ stress of rock mass around the chamber is initialized by using the quasi-static method, as discussed in Section 2.1.

2.4.2 Result comparison

Figure 5 compares time histories of measured and simulated pressure at the monitoring location shown in Fig. 4. It can be seen that the simulated one matches well with the measured one in terms of the peak pressure and the waveform. The good agreement between the measured and simulated pressures indicates that the material models and

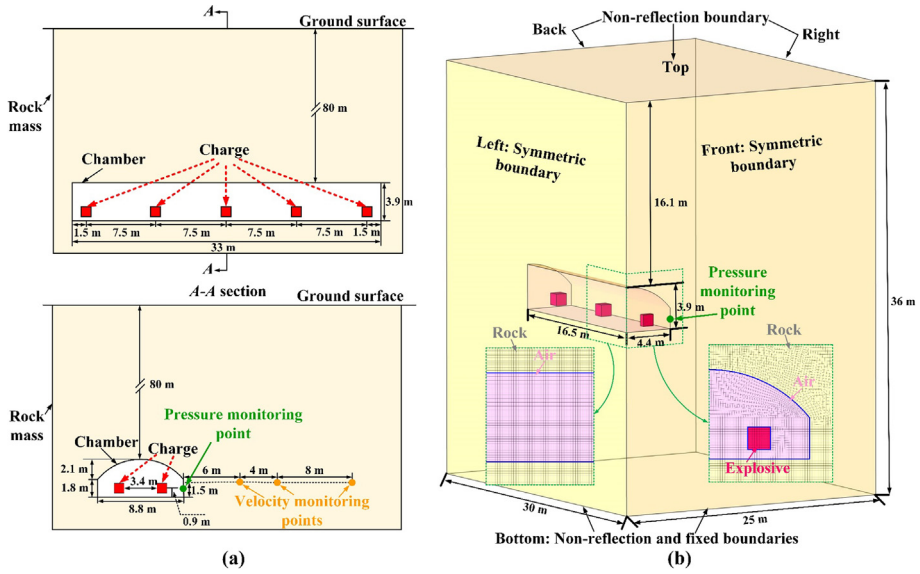

Fig. 4. (a) Test setup (Wu, Lu, et al., 2003), and (b) numerical model.

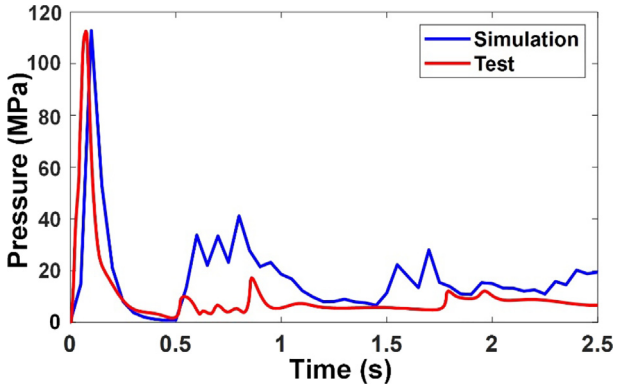

Fig. 5. Measured (Zhou et al., 2002) and simulated pressure at the monitoring location.

EOS of air and explosive can accurately predict explosion loads acting on the chamber wall.

Figure 6 shows the measured and simulated velocity time histories and the corresponding frequency spectra at the three monitoring locations. It is found that the simulated velocities including peaks and waveforms agree well with the measured ones at three monitoring locations (see Fig. 6(a)). The oscillations at the tails of simulated velocity histories can be observed, while the measured ones at the three monitoring locations do not have obvious tail oscillations. The main reason is that the numerical model does not include site geological discontinuities with the ability to absorb stress wave energy. In addition, the Fourier spectra of velocity–time histories (see Fig. 6(b)) show that the main frequency bands of simulated vibration components at the three monitoring points agree well with the corresponding measured ones. In summary, the RHT material model can well represent the rock mass material properties in predicting the vibration responses of the rock mass (i.e., intensity, duration, and frequency) subjected to explosions inside underground openings.

3 Comparison of vibrations induced by BLEVE and TNT explosion

With calibrated numerical models, the vibration characteristics caused by the LPG BLEVE and its TNT-equivalence explosion are compared in this section. Risk evaluations of the LPG BLEVE-induced vibrations and TNT explosion-induced vibrations are also conducted. The details are given below.

3.1 Analysis of vibration characteristics

The vibrations induced by the LPG BLEVE are compared with those calculated from the equivalent TNT explosion inside the tunnel. Figure 7 shows the radial velocity time histories and the corresponding time–frequency-power spectra at the monitoring point with the scaled distance of 0.67 m/kg$^{1/3}$ from the LPG BLEVE and TNT explosion centre (7 m from the explosion centre, i.e., the monitoring point closest to the explosion centre among all monitoring points arranged in Figs. 1 and 2). It should be noted that the TNT equivalence weight is used to calculate the scaled distance under LPG BLEVE. As shown in Fig. 7(a) and (b), the peak vibration velocity at the monitoring point induced by the TNT explosion is significantly higher than that induced by the LPG BLEVE, i.e., about 2.2 m/s vs. 0.27 m/s, due to the higher TNT explosion pressure (see Fig. 3). Meanwhile, the main vibration energy induced by the TNT explosion is distributed near the frequency of 250 Hz, whereas that from the LPG BLEVE concentrates around the frequency of 50 Hz due to the characteristics of LPG BLEVE load with a slower loading rise and longer duration (see Fig. 3). Accordingly, it can be concluded that although the intensity of vibrations induced by the LPG BLEVE is lower than that generated by the equivalent TNT explosion, the

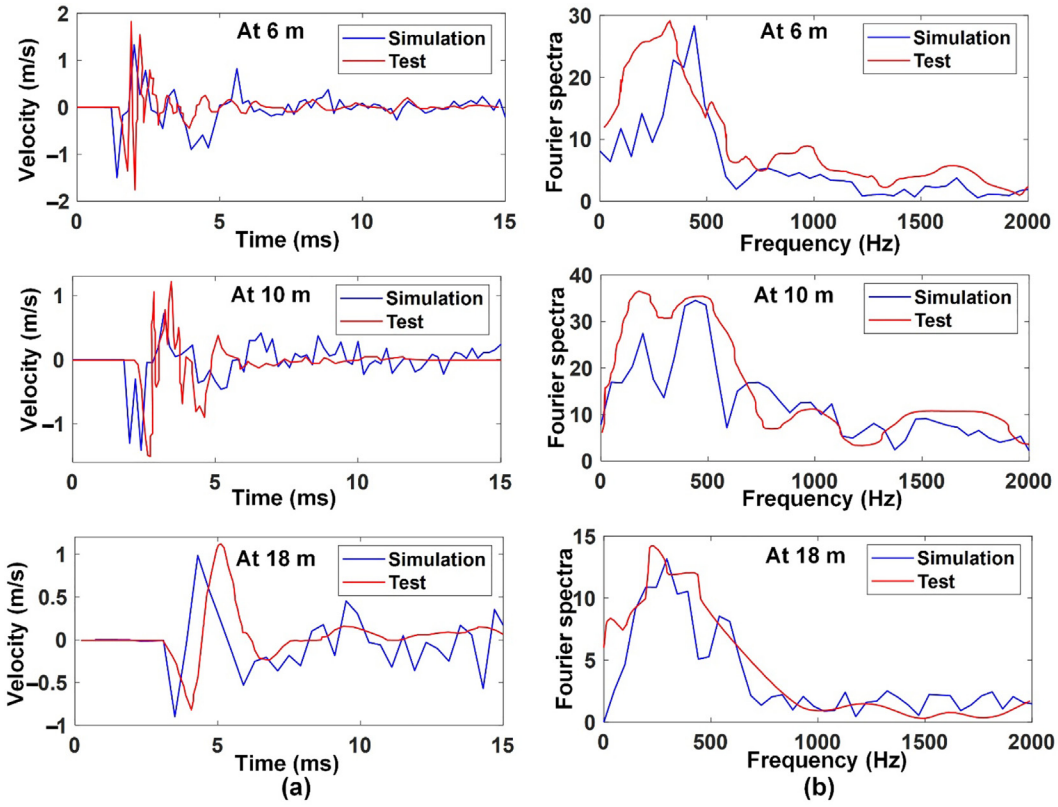

Fig. 6. Comparison of measured and simulated vibration responses of rock mass at three velocity monitoring locations (6, 10, and 18 m) (Wu et al., 2003; Zhou et al., 2002; Zhou & Jenssen, 2009). (a) Velocity–time histories, and (b) frequency spectra.

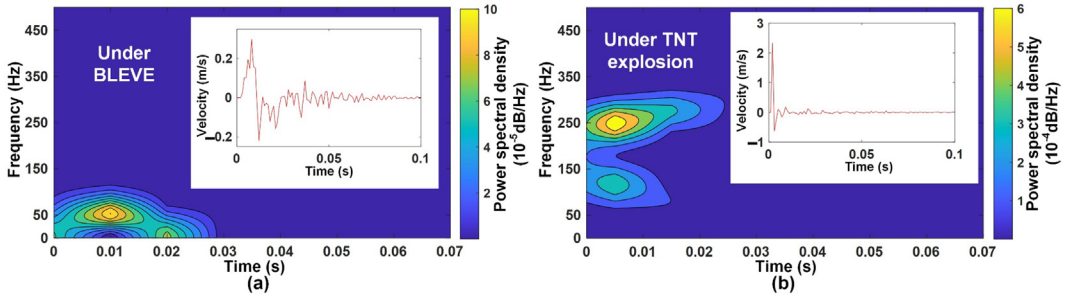

Fig. 7. Time-frequency-power spectral densities of radial velocity time histories induced by (a) LPG BLEVE, and (b) TNT explosion at 0.67 m/kg$^{1/3}$ scaled distance from the explosion centre.

damage risk of LPG BLEVE-induced vibration is not necessarily lower than that of TNT explosion-induced vibration. The main reason is that LPG BLEVE-induced vibrations are mainly distributed in relatively low frequency bands. Therefore, it is essential to examine the risk of vibrations caused by the TNT explosion and LPG BLEVE through evaluating intensity and frequency of the two types of vibrations.

In existing studies, peak particle velocity (PPV) is widely used as the intensity indicator of blast-induced vibrations. In fact, both stress and PPV can reflect the intensity of blast-induced stress waves. PPV divided by wave propagation velocity is equal to strain in theory, which is proportional to stress through material elastic modulus. Normally, with the propagation of blast-induced stress waves inside rock mass, their PPVs and stresses gradually decrease. At the free surface, PPVs and stresses (e.g., tensile stresses) of blast-induced stress waves can both be intensified due to the reflection effect of stress waves at the free surface. Therefore, PPVs and stresses are correlated positively. There are two types of PPV, i.e., the maximum among the velocity time histories in the three directions and the maximum resultant velocity. The two types of PPV are both utilized herein to compare the vibration intensities induced by the TNT explosion and LPG BLEVE. A typical empirical formula based on the site constants and the scaled distance, is employed to evaluate the attenuation characteristics of two types of PPV, as given in

Eq. (1) (North Atlantic Treaty Organization [NATO], 2010):

$$\mathrm{PPV} = k \times \left(L/w^{1/3}\right)^{-b}, \tag{1}$$

where k is the initial coefficient; b is the attenuation coefficient; L is the standoff distance; w is the equivalent explosive weight.

Figure 8(a) and (b) shows the two types of PPVs at the nine monitoring points and their best fits based on Eq. (1). The curve fitted for TNT explosion-induced PPVs is obtained by ensuring the minimal error sum between simulated data and the fitted curve. The difference between the fitted curve and simulated data in Fig. 8(a) seems large, which is due to the fact that the fitted curve is shown based on the logarithm of the original data. In fact, the maximum error between simulated data and the fitted curve is less than 0.1 m/s at scaled distances larger than 1.3 m/kg$^{1/3}$. The curves fitted based on the original data in the sub-figures of Fig. 8(a) show that the fitted curve agrees well with the simulated data. It can be seen that the two types of PPVs induced by the TNT explosion and LPG BLEVE both decrease with the increase in scaled distance. For the same type of explosion, the calculated resultant PPV fits Eq. (1) better than the maximum PPV (see squared correlation coefficient R^2 in Table 3). The attenuation coefficient of PPVs of the resultant velocity under TNT explosion is 3.06, i.e., over 3.8 times that of LPG BLEVE-induced PPVs. The results indicate that TNT explosion-induced PPVs attenuate more quickly than LPG BLEVE-induced ones. In addition, TNT explosion-induced resultant PPV is higher than LPG BLEVE-induced resultant PPV at the same scaled distances less than 1.68 m/kg$^{1/3}$. However, the opposite is observed, i.e., LPG BLEVE-induced ground vibration PPV becomes larger when the scaled distance is greater than 1.68 m/kg$^{1/3}$.

In addition to the intensity, dominant frequency (DF), principal frequency (PF), and average frequency (AF) as the frequency indicators have been widely used to evaluate the frequency characteristics of blast-induced vibrations. DF is defined as the frequency corresponding to the peak $F_{\max}$ in the Fourier spectrum of velocity–time history (see Fig. 9). PF is defined as the average of two frequencies corresponding to the half peak in the Fourier spectrum of velocity–time history, as given in Eq. (2) (Wu et al., 2003), and AF is determined by Eq. (3) (Triviño et al., 2012).

$$\mathrm{PF} = \frac{f_1 + f_2}{2}, \tag{2}$$

$$\mathrm{AF} = \frac{\sum_{i=1}^{m} F_i f_i}{\sum_{i=1}^{m} F_i}, \tag{3}$$

where f_1 and f_2 are the frequencies corresponding to the half peak $F_{\max}/2$ in the Fourier spectrum, as shown in Fig. 9; F_i is the amplitude corresponding to the frequency f_i in the Fourier spectrum; m is the total number of data pairs in the Fourier spectrum. It is noted that the PF in Fig. 9 is larger than the corresponding DF. However, PFs of LPG BLEVE-induced ground vibrations are not necessarily larger than DFs of the same ground vibrations due to varied characteristics of different velocity time histories of ground vibrations.

PF, AF, and DF are all used herein to evaluate the frequency characteristics of ground vibrations caused by the TNT explosion and LPG BLEVE. A typical empirical formula based on the site constants and the scaled distance is employed to evaluate the attenuation characteristics of the three types of frequency definitions, as given in Eq. (4) (NATO, 2010):

$$f = n \times \left(L/w^{1/3}\right)^{-m}, \tag{4}$$

where n is the initial coefficient; m is the attenuation coefficient; L is the standoff distance; w is the equivalent explosive weight; f is the frequency indicator, i.e., PF, AF, or DF.

As shown in Fig. 1(a), nine vibration monitoring points are arranged at the same level of the explosion centre along the horizontal direction. The vibrations are more significant in the radial direction (i.e., the horizontal direction)

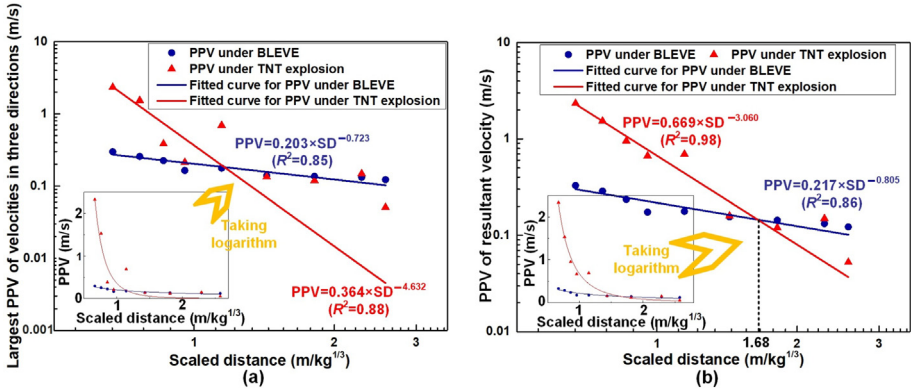

Fig. 8. Two types of PPVs at different scaled distances. (a) The largest PPVs of velocity time histories in the three perpendicular directions, and (b) PPVs of resultant velocity time histories. Note: The lines are fitted based on the logarithm of the original data. The curves in the sub-figures are fitted based on the original data.

Table 3
Initial coefficient (k), attenuation coefficient (b), and squared correlation coefficient for empirical fits of PPVs.

PPV type	Explosion category	k	b	R^2
The largest PPV among the velocities in three directions	LPG BLEVE	0.203	0.723	0.85
	TNT explosion	0.364	4.632	0.88
PPV of the resultant velocity	LPG BLEVE	0.217	0.805	0.86
	TNT explosion	0.669	3.060	0.98

Note: R^2 is the squared correlation coefficient between fitted and simulated data.

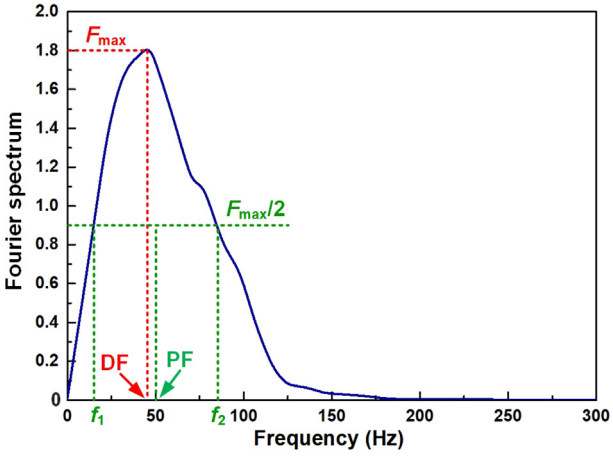

Fig. 9. Definition of principle frequency (PF) and dominant frequency (DF).

than the other two directions. Therefore, three frequencies (i.e., PF, AF, and DF) of velocity time histories in radial direction under the TNT explosion and LPG BLEVE are compared herein, as shown in Fig. 10. It can be found that PFs, AFs, and DFs of vibrations induced by the LPG BLEVE and TNT explosion all decrease with the increase of scaled distance. Although the three types of frequencies of ground vibrations induced by the TNT explosion attenuate slightly faster than the corresponding ones induced by the LPG BLEVE (see coefficient m in Table 4), three types of ground vibration frequencies from the TNT explosion are all significantly higher than those from the LPG BLEVE in the monitored scaled distance range (see Fig. 10). In addition, it can be found that the fitted curves for PF corresponding to the LPG BLEVE and TNT explosion have better correlations with the simulated data as compared to the ones in the cases of AF and DF (see squared correlation coefficient R^2 in Table 4).

3.2 Evaluation of vibration risk induced by LPG BLEVE and TNT explosion

The above analysis compares the vibration characteristics of free-field rock mass around of tunnel caused by

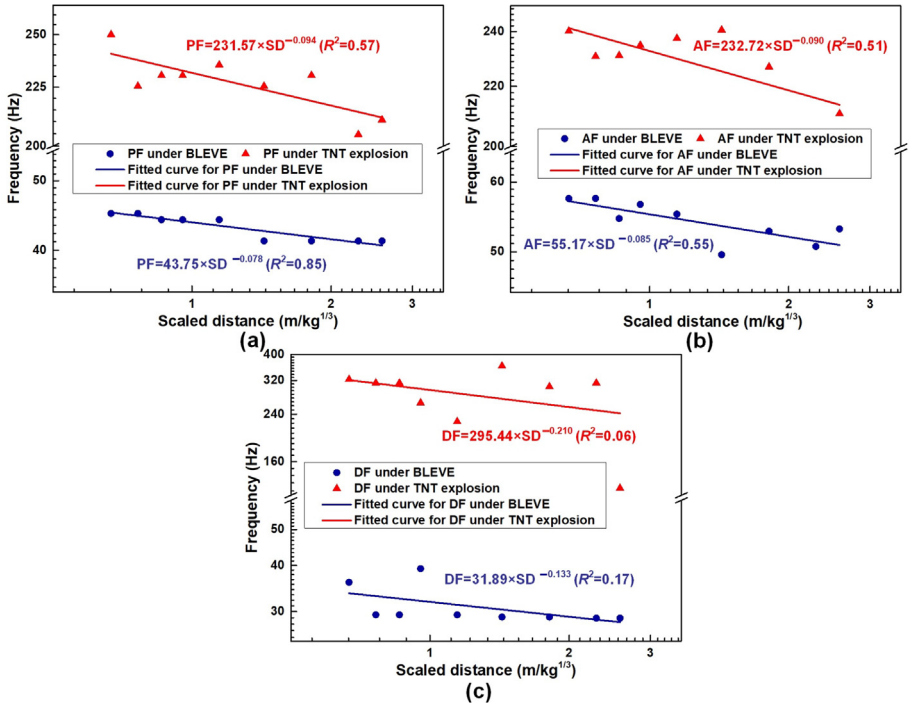

Fig. 10. PFs, AFs, and DFs and their best fit curves versus scaled distance. (a) PFs versus scaled distance, (b) AFs versus scaled distance, and (c) DFs versus scaled distance.

Table 4
Initial coefficient (n), attenuation coefficient (m), and squared correlation coefficient for empirical fits of PF, AF, and DF.

Frequency type	Explosion category	n	m	R^2
PF	LPG BLEVE	43.75	0.078	0.85
	TNT explosion	231.57	0.094	0.57
AF	LPG BLEVE	55.17	0.085	0.55
	TNT explosion	232.72	0.090	0.51
DF	LPG BLEVE	31.89	0.133	0.17
	TNT explosion	295.44	0.210	0.06

Note: R^2 is the squared correlation coefficient between the fitted curve and simulated data.

the TNT explosion and LPG BLEVE. When stress waves in rock mass encounter existing underground structures (e.g., adjacent tunnels), stress waves are reflected at the free surfaces of adjacent underground structures and intensified. Thus, to assess the explosion effect on adjacent tunnels, it is necessary to consider the reflection effect of free surfaces of adjacent underground structures on the intensity and frequency of blasting vibrations for an accurate risk assessment of blasting vibrations. Subsequently, the numerical model of twin tunnels is developed by incorporating an adjacent tunnel into the existing numerical models of the road tunnel in Section 2, thereby investigating the influence of the surface reflection on blasting vibration characteristics. The adjacent tunnel has the same geometry, structural configurations, mesh details, and material models as the existing tunnel in Section 2.

Furthermore, the adjacent tunnel is arranged at different distances (i.e., 4, 6, 9, 13, 18, and 21 m) from the existing tunnel to investigate the reflection effects of free surfaces at different distances on blasting vibrations. The blasting vibration at the inner surface of the adjacent tunnel in each case is compared with that at the same distance in free-field rock mass from the explosion center. Figure 11 shows the case of twin tunnels with the spacing of 4 m and the case of a single tunnel under the same internal LPG BLEVE.

Figures 12 and 13 respectively show the LPG BLEVE and TNT explosion-induced vibrations at the inner surface of the adjacent tunnel with different spacings of twin tunnels, which are compared with those in rock mass at the corresponding locations in the case without the adjacent tunnel. PFs of radial components and PPVs of resultant velocity are used as indicators for comparison. It can be seen that PFs of blast vibrations at the inner surface of the adjacent tunnel are slightly higher than those at the same location in free-field rock mass under the same internal explosion. The results indicate that free surface of the adjacent tunnel has very limited influence on PF of blast vibrations. On the contrary, the reflection of the free surface on stress waves significantly intensifies the PPV of blast vibrations. The LPG BLEVE-induced PPV at the inner surface of the adjacent tunnel with the spacing of 4 m is over three times that at the corresponding location in rock mass without the adjacent tunnel. With the separation distance of 6 m or more between two tunnels, LPG BLEVE-induced PPV at the inner surface of the adjacent tunnel is approximately twice that at the corresponding locations in rock mass. Under TNT explosion, the vibration intensity at the inner surface of the adjacent tunnel with a separation distance of 6 m or less is over three times that at the corresponding location in rock mass. When the spacing of twin tunnels reaches 9 m or more, the free-surface amplification coefficient (i.e., the ratio of PPVs at the surface of adjacent tunnel to that in rock mass at the

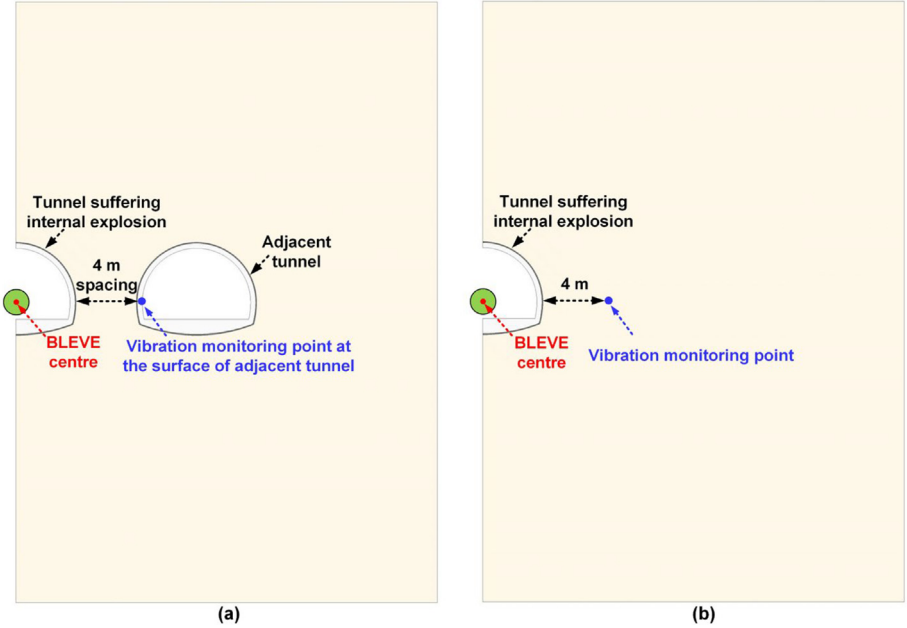

Fig. 11. Numerical models of road tunnel under the same internal LPG BLEVE (a) with an adjacent tunnel, and (b) without an adjacent tunnel and the corresponding vibration monitoring arrangements.

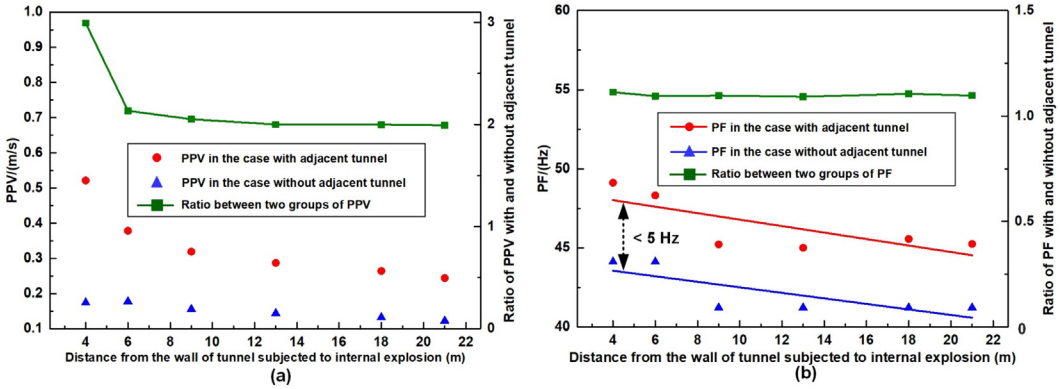

Fig. 12. Comparison of LPG BLEVE-induced vibrations at the inner surface of adjacent tunnel and in rock mass without adjacent tunnel. (a) PPV comparison, and (b) PF comparison.

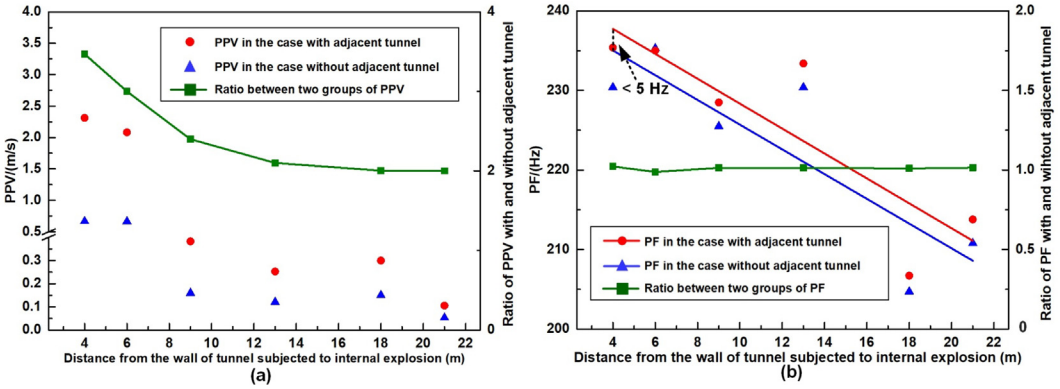

Fig. 13. Comparison of TNT explosion-induced vibrations at the inner surface of the adjacent tunnel and in rock mass without the adjacent tunnel. (a) PPV comparison, and (b) PF comparison. Note: the slightly higher PPV at the distance of 18 m may be due to the influence of unloading-induced vibrations (Cao et al., 2016) after blast loading.

same scaled distance) is reduced to about two. The results show the vibration intensity (i.e., PPV) under the TNT explosion is more significantly intensified by the surface reflection. This is because shock waves induced by the TNT explosion propagate faster than those induced by the LPG BLEVE, as shown in Fig. 14. The shock waves with higher velocity can be more significantly reflected by the free surface and are therefore more significantly intensified. When the wave velocity is that of elastic wave of the rock mass (see Fig. 14), the amplification coefficient is about 2.0 when wave incident angle to the surface is zero (see Figs. 12 and 13).

Figure 15 shows LPG BLEVE and TNT explosion-induced PPVs (versus PFs and scaled distances) at the inner surface of the adjacent tunnel with different spacings (i.e., 4, 6, 9, 13, 18, and 21 m). PPVs under LPG BLEVE and TNT explosion are fitted based on Eq. (1), as shown in Fig. 15(a). It can be seen that LPG BLEVE-induced PPVs attenuate more slowly than TNT explosion-induced ones, which leads to the TNT explosion-induced PPVs being initially higher than LPG BLEVE-induced PPVs, then lower than those induced by LPG BLEVE after a certain scaled

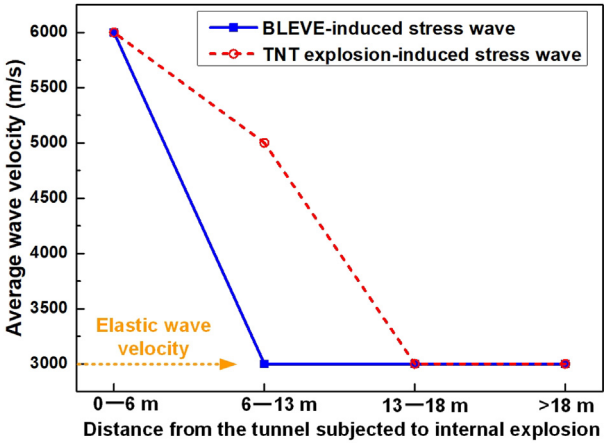

Fig. 14. Wave velocities in rock mass caused by LPG BLEVE and TNT explosion.

distance. This variation of PPVs at the surface of adjacent tunnels is similar to that in free-field rock mass, as discussed in Section 3.1.

To evaluate the damage risk of vibrations induced by the LPG BLEVE and TNT explosion, these vibration data

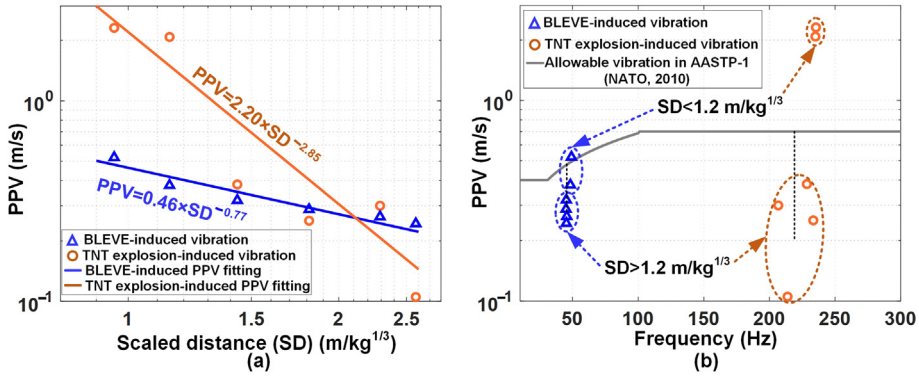

Fig. 15. (a) Vibrations induced by LPG BLEVE and TNT explosion, and (b) their comparisons with the allowable vibration specified in AASTP-1 (NATO, 2010).

is compared with the allowable vibrations specified in AASTP-1 (NATO, 2010) (see Eq. (5)), which considers wide frequency ranges and gives clear critical PPV limits at different frequencies. It can be found from Fig. 15(b) that when the scaled distance is less than 1.2 m/kg$^{1/3}$ (i.e., twin tunnels with the spacing of 6 m in this study), vibrations induced by the TNT explosion are far over the allowable vibration limit, while LPG BLEVE-induced vibrations are slightly above or near the allowable vibrations. On the other hand, when the scaled distance is greater than 1.2 m/kg$^{1/3}$, vibrations induced by the TNT explosion and LPG BLEVE are below the allowable vibrations. In this case, the LPG BLEVE-induced vibrations are close to the allowable vibrations than those induced by the TNT explosion. The results reveal that the vibrations induced by the TNT explosion have higher damage risks to adjacent tunnels with the scaled distance of less than 1.2 m/kg$^{1/3}$. In comparison, LPG BLEVE-induced vibrations have higher risks to adjacent structures with the scaled distance greater than 1.2 m/kg$^{1/3}$.

$$\begin{cases} \text{PPV} \leqslant 0.4 \text{ m/s for } 10 \text{ Hz} \leqslant \text{PF} \leqslant 30 \text{ Hz} \\ \text{PPV} \leqslant 0.0825 \times \text{PF}^{0.46} \text{ m/s for } 30 \text{ Hz} \leqslant \text{PF} \leqslant 100 \text{ Hz} \\ \text{PPV} \leqslant 0.7 \text{ m/s for } 100 \text{ Hz} \leqslant \text{PF} \end{cases} \tag{5}$$

The difference of ground vibrations induced by the LPG BLEVE and TNT equivalence explosion is attributed to the different characteristics of the two blast loads acting on the inner wall of the tunnel. TNT-equivalence explosion loads have higher peak overpressures, less impulses, and shorter durations and rise time than BLEVE-induced loads, as shown in Fig. 3. TNT explosion loads with higher peak overpressures and faster loading rise can induce ground vibrations with higher intensity near the explosion and higher frequencies. TNT explosion-induced ground vibrations with higher frequency attenuate more rapidly than BLEVE-induced ground vibrations since high-frequency waves are more likely to attenuate and are easier to be filtered out by ground media.

4 Parametric study under LPG BLEVE

As discussed above, LPG BLEVE-induced ground vibrations are different from TNT explosion-induced vibrations. The vibrations induced by TNT explosions have been intensively investigated. However, some key factors influencing LPG BLEVE-induced vibrations have not been investigated in existing studies. In the present study, the effects of the cover depth of tunnel, surrounding rock type, rock porosity, and concrete wall grade on LPG BLEVE-induced vibrations are further investigated. It is noted that at the same scaled distance, the intensities of vibrations at the surface of the adjacent tunnels are larger than those in the free-field rock mass owing to wave reflection at the adjacent tunnel surface, as reported in Section 3.1. Meanwhile, the frequencies of the vibrations at the surface of the adjacent tunnels are close to those in the free-field rock mass at the same scaled distance. Furthermore, blast vibrations in free-field rock mass have similar attenuation trends as those at the surface of the adjacent tunnels with different distances from the left tunnel, as illustrated in Section 3.2. Therefore, when the spacing of adjacent tunnels is over a certain distance (e.g., 6 m in Section 3.2), i.e., the intensity of LPG BLEVE-induced vibrations can be attenuated below the elastic limit of the rock mass before the stress waves reach the surface of the adjacent tunnels (i.e., the velocity of stress waves is that of elastic waves), the effects of the above-mentioned factors on the vibrations in the free-field rock mass can reflect those at the surface of adjacent tunnels. The effects of various factors on LPG BLEVE-induced vibrations in free-field rock mass are thus investigated in this section. PPVs of resultant velocity and PFs of radial velocity are used as indicators of LPG BLEVE-induced vibrations. Based on the site investigation (Yang, 2006), the rock mass around the tunnel is of good quality and relatively intact. Therefore, the effect of rock mass discontinuity on ground vibrations is not considered and the rock mass around the tunnel is assumed intact. Four factors (i.e., cover depth, rock type, rock porosity, and lining concrete grade) significantly influencing TNT

explosion-induced ground vibrations are considered in this section to examine their effects on LPG BLEVE-induced ground vibrations.

4.1 Effect of cover depth

In Section 2, the LPG BLEVE-induced vibration of rock mass around the arched tunnel with a cover depth of 100 m is investigated. To examine the influence of cover depth on LPG BLEVE-induced vibrations, five cover depths (i.e., 10, 30, 50, 100, and 500 m) are respectively incorporated into numerical models of the single-arched tunnel. It is noted that the cover depth in this study is measured from the tunnel centre to the ground surface. These five numerical models have the same structural and geometric configurations of tunnel, element types and sizes, material models, and vibration monitoring arrangements, as described in Section 2. The arched tunnels in five numerical models are subjected to the same internal LPG BLEVE as shown in Section 2.1. In-situ stresses of rock mass with five cover depths are obtained based on empirical equations and are then incorporated into numerical models using the quasi-static method, as discussed in Section 2.1.

Figure 16 shows PPVs and PFs of LPG BLEVE-induced vibrations at monitoring locations inside rock mass (see Fig. 1) corresponding to the five cover depths. The empirical fits for PPVs and PFs in different cases are also given in Fig. 16. It can be seen that at the same scaled distances, PPVs significantly decrease with the increase in cover depth from 10 to 30 m, as shown in Fig. 16(a). This is because with the increase of tunnel cover depths, the effects of ground-surface reflection on LPG BLEVE-induced vibration response inside rock mass gradually reduce. Furthermore, PPVs at the same scaled distances slightly decrease as the cover depth increases from 30 to 50 m but greatly increase as the cover depth increases from 50 to 500 m. It is because increasing cover depth, i.e., increasing in-situ stress of rock mass, can reduce rock vibration intensity owing to incremental constraints of rock mass and decreased surface reflection. However, a further increase in the in-situ stress of the rock mass with increasing cover depth can increase the vibration intensities of the rock mass, possibly because the high in-situ stress can induce more significant unloading vibrations of the rock mass towards the tunnel after LPG BLEVE loading. In addition, PFs of vibrations at the same scaled distance always reduce as the cover depth increases from 10 to 500 m, as shown in Fig. 16(b). The results reveal that increasing cover depth, i.e., increasing the in-situ stress, can effectively suppress the high-frequency components of vibrations.

To evaluate the effect of cover depths on the LPG BLEVE-induced vibrations, it is necessary to consider both the frequency and intensity of LPG BLEVE-induced vibrations. Since the blast vibrations inside rock mass without an adjacent tunnel have similar variation trends as those at the surface of the adjacent tunnel at different distances subjected to internal LPG BLEVE, the effect of cover depths on LPG BLEVE-induced ground vibrations at the surface of adjacent tunnel can be indicated by ground vibrations inside rock mass. Figure 17 compares the monitored vibrations (i.e., PPVs and PFs) inside rock mass for the cases of five cover depths. It can be found that the monitored vibrations in free-field rock mass with 10 m cover depth are the closest to the allowable vibrations among the five cases. Meanwhile, the monitored vibrations with 30 m cover depth are the most deviated from the allowable vibrations in general. Moreover, as the cover depth increases from 30 to 500 m, the distance from the monitored vibrations to the allowable vibrations gradually decreases. The results show that 30 m is the best cover depth of the tunnel in the sandstone to minimize the risk of LPG BLEVE-induced vibrations.

4.2 Effect of rock type

The above discussions focus on LPG BLEVE-induced vibrations inside the sandstone. However, different categories of rock mass can surround the arched tunnel along its longitudinal alignment, as reported by Yang (2006). Therefore, it is necessary to investigate LPG BLEVE-induced vibration responses of different types of rock mass around the arched tunnel. In this section, numerical models

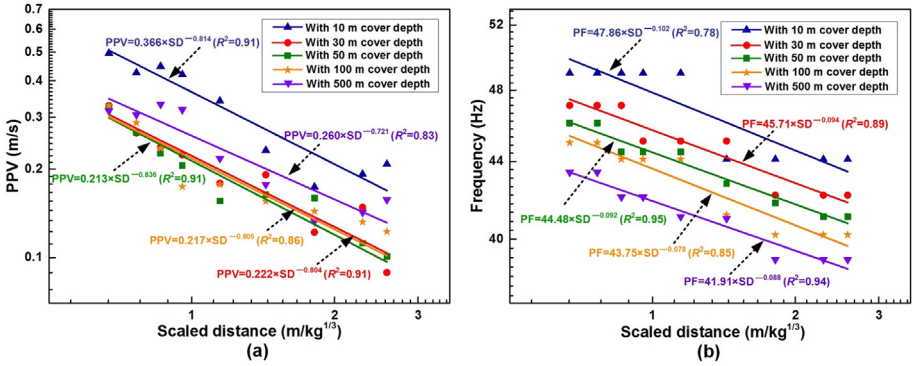

Fig. 16. PPVs and PFs of LPG BLEVE-induced vibrations at different scaled distances and the corresponding empirical relations with different cover depths. (a) PPVs and their best fits, and (b) PFs and their best fits.

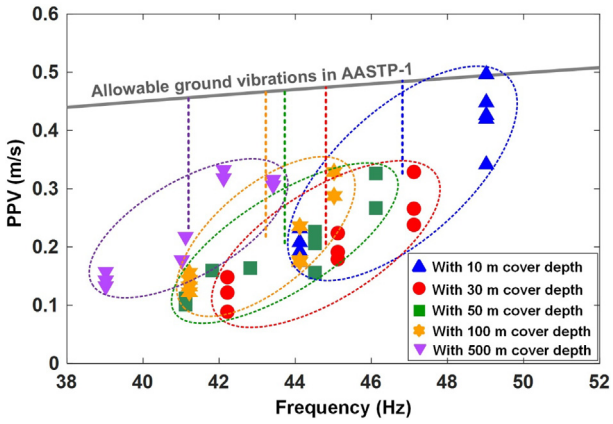

Fig. 17. Comparison of LPG BLEVE-induced vibrations in the cases of five cover depths with the vibration criteria specified in AASTP-1 (NATO, 2010).

of the arched tunnel surrounded by three rock masses, i.e., mudstone, conglomerate, and sandstone, are respectively built to investigate their effects on vibration characteristics induced by the same LPG BLEVE in the tunnel with a 30 m cover depth. Three numerical models with different rock categories have the same geometric configurations, element details, boundary conditions, lining model parameters, and monitoring arrangements. The parameters of RHT model for different categories of rock mass are sourced from the field test data (Yang, 2006), empirical equations (Liu et al., 2018), and relevant references (Liu et al., 2018; Xie et al., 2017). Table 5 lists different values of RHT model parameters for the three categories of rock mass. The remaining RHT model parameters are set to be the same as those given in Table 2.

Figure 18 shows PPVs and PFs of LPG BLEVE-induced vibrations at different scaled distances and the corresponding fitted empirical relations for the three types of rock mass. It can be seen from Fig. 18(a) that with the enhanced mechanical properties of rock mass (i.e., rock mass varying from mudstone, conglomerate to sandstone), PPVs of vibrations reduce at the same scaled distance. Moreover, with the increased scaled distance, PPVs of vibrations reduce more significantly when rock mass is changed from sandstone and conglomerate to mudstone (i.e., decreased mechanical properties of rock mass) due to the increased rock damping actions (Zhang et al., 2005). Meanwhile, PFs of LPG BLEVE-induced vibrations at the same scaled distance increase with the enhanced mechanical properties of rock mass (i.e., rock mass varying from mudstone and conglomerate to sandstone), as shown in Fig. 18(b). This is mainly because rock mass with enhanced mechanical properties has higher modulus, and thus facilitates more vibration energy distributed in the higher frequency ranges.

Figure 19 compares LPG BLEVE-induced vibrations in the three types of rock mass with the allowable vibration limits. As shown, many calculated PPVs in mudstone are above the allowable vibrations, while all the calculated PPVs in sandstone are below the allowable vibration limits. In conglomerate, only one calculated PPV is above the allowable vibration limit, while the others are all smaller than the allowable vibration limit. These results show that the LPG BLEVE-induced vibrations in mudstone are larger than those in the other two considered rock masses, and could be higher than the allowable vibrations. Therefore, special attention should be paid to avoid damage to adjacent underground and above-ground structures by accidental explosions if the road tunnel is constructed in mudstone or in soft rock in general.

4.3 Effect of rock porosity

The porosity of rock mass is defined as the ratio of pore volume inside the rock mass to rock mass volume. The above analysis discusses the vibration response of rock mass with zero porosity, i.e., without porosity. To investigate the effect of rock porosity on LPG BLEVE-induced vibrations, numerical models of single-arched tunnel with different rock porosities are built herein to be subjected to the same internal LPG BLEVE as described in Section 2.1. For ease of comparison, uniformly-distributed pores with the same individual geometry and volume are considered and defined for the rock mass with different porosities. The arched tunnel in sandstone with a cover

Table 5
RHT model parameters for the three types of rock mass (Yang, 2006; Liu et al., 2018; Xie et al., 2017).

Type of parameter	Specific parameter	Rock type		
		Sandstone	Conglomerate	Mudstone
Basic parameters	Density (kg/m^3)	2600	2604	2650
	Compressive strength (MPa)	41.0	32.5	15.3
	Elastic shear modulus (GPa)	28.0	18.7	8.2
Strain rate parameters	Compressive strain rate dependence exponent β_c	0.028	0.034	0.061
	Tensile strain rate dependence exponent β_t	0.033	0.038	0.057
Strength parameters	Failure surface parameter A	2.70	2.73	2.86
	Failure surface parameter N	0.65	0.64	0.62
EOS parameters	Crush pressure P_{el} (MPa)	27.33	21.81	10.25
	Hugoniot polynomial coefficient A_1 (GPa)	25.36	33.04	18.32
	Hugoniot polynomial coefficient A_2 (GPa)	37.34	48.55	26.92
	Hugoniot polynomial coefficient A_3 (GPa)	21.00	21.12	11.71

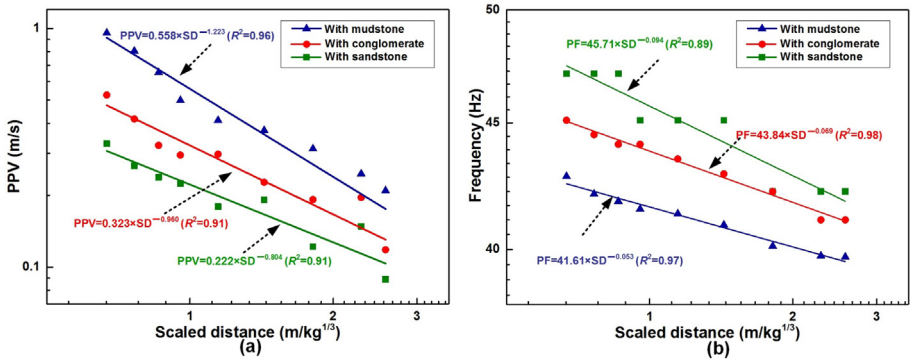

Fig. 18. PPVs and PFs of LPG BLEVE-induced vibrations at different scaled distances and the corresponding best-fitted empirical relations in the three types of rock mass. (a) PPVs and their best fits, and (b) PFs and their best fits.

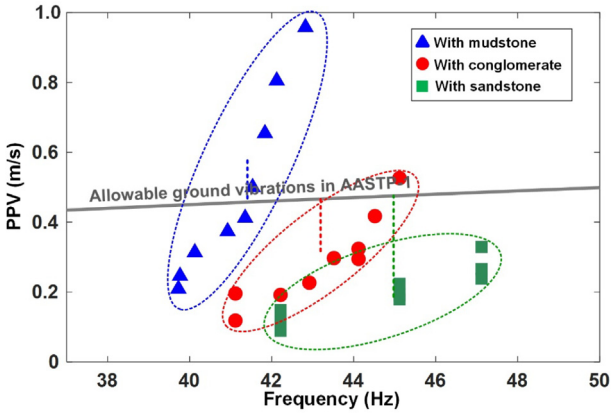

Fig. 19. Comparison of LPG BLEVE-induced vibrations in three types of rock mass with the vibration criteria specified in AASTP-1 (NATO, 2010).

depth of 30 m is selected in this section. The sandstone porosity is normally lower than 30% (Domenico, 1984). Therefore, the numerical models with three rock porosities (i.e., 0%, 16.7%, and 28.9%) are respectively built. The models have the same geometric configurations, element details, boundary conditions, lining model parameters, and monitoring arrangements, as those in Section 2. It is noted that the strength, stiffness, and strain rate sensitivity of the porous rock mass is affected by the variation of rock porosity. Therefore, the corresponding parameters of the *MAT_RHT under different rock porosities should be adjusted to reflect the effect of rock porosity on rock mass properties. In this study, based on the mechanical parameters of rock with 0% porosity (Yang, 2006), the strengths and moduli of rock mass with the porosities of 16.7% and 28.9% are calculated by using the empirical relations proposed by Mukerji et al. (1995) and Vernik et al. (1993). The other parameters of the *MAT_RHT model that influence the rock mass response are obtained based on Liu et al. (2018), as given in Table 6. The remaining parameters are set to be the same as those in Table 2.

Figure 20 shows the PPVs and PFs of LPG BLEVE-induced vibrations at different scaled distances and the corresponding fitted empirical relations for three rock porosities. It can be seen that with the increased scaled distance, the PPVs of vibration reduce more significantly in rock mass with higher porosity. The PPVs of vibrations at the same scaled distance are lower when the rock porosity is lower, as shown in Fig. 20(a). This is because the enhanced rock mechanical properties with the lower rock porosity can more effectively reduce the rock mass response to LPG BLEVE load (i.e., the PPVs inside rock mass near the tunnel). As shown in Fig. 20(b), PFs of LPG

Table 6
RHT model parameters for the three types of rock mass (Liu et al., 2018; Mukerji et al., 1995; Vernik et al., 1993; Yang, 2006).

Type of parameter	Specific parameter	Rock porosity		
		0%	16.7%	28.9%
Basic parameters	Density (kg/m^3)	2600.0	2165.8	1848.6
	Compressive strength (MPa)	41.0	12.4	1.9
	Elastic shear modulus (GPa)	28.0	9.5	2.5
Strength parameters	Failure surface parameter A	2.70	2.90	3.38
	Failure surface parameter N	0.65	0.62	0.56
Strain rate parameters	Tensile strain rate dependence exponent β_t	0.033	0.062	0.091
	Compressive strain rate dependence exponent β_c	0.028	0.070	0.156
EOS parameters	Initial porosity parameter	1.0	1.2	1.4
	Crush pressure P_{el} (MPa)	27.33	8.27	1.27
	Hugoniot polynomial coefficient A_1 (GPa)	25.36	11.40	3.50
	Hugoniot polynomial coefficient A_2 (GPa)	37.34	16.79	5.15
	Hugoniot polynomial coefficient A_3 (GPa)	21.00	9.44	2.90

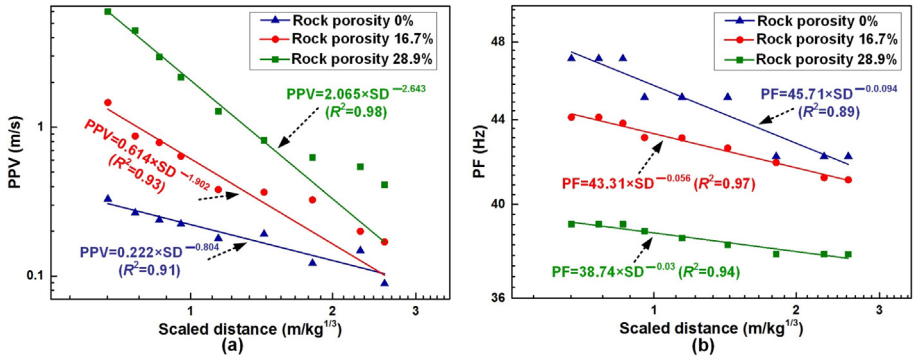

Fig. 20. PPVs and PFs of LPG BLEVE-induced vibrations at different scaled distances and the corresponding empirical fitted relations under three rock porosities. (a) PPVs and their best fits, and (b) PFs and their best fits.

BLEVE-induced vibrations at the same scaled distance decrease with the increase of rock porosity (i.e., the weakened mechanical property) due to the reduced rock stiffness.

Figure 21 compares the LPG BLEVE-induced vibrations inside rock mass of the three rock porosities with the allowable vibration limits. As shown, rock mass with high porosities experiences larger vibrations under the same LPG BLEVE loads. The vibration levels of rock mass with 28.9% porosity are almost all larger than the allowable vibration limit, followed by those in rock mass with 16.7% porosity. The calculated PPVs in the rock mass with 0% porosity are all below the allowable vibration limit. These results indicate that special attention should be paid to vibration control to avoid damage to adjacent structures from an accidental LPG BLEVE inside the tunnel, which was constructed in rock mass with high porosities.

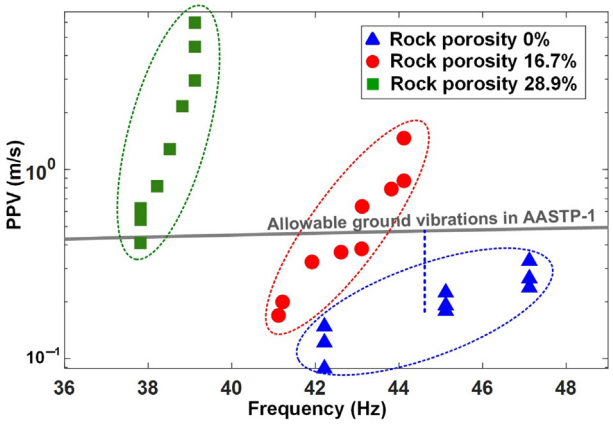

Fig. 21. Comparison of the allowable vibration specified in AASTP-1 with LPG BLEVE-induced vibrations in rock mass with three rock porosities with (NATO, 2010).

4.4 Effect of concrete grade

The above results are obtained based on numerical studies of the arched tunnel with 25 MPa compressive strength of lining concrete (i.e., C25 concrete). To examine the effects of concrete grades on LPG BLEVE-induced vibrations, numerical models of single-arched tunnel with five concrete grades (i.e., C15, C25, C35, C45, and C55) are built in sandstone with a cover depth of 30 m. Other parameters including configurations, material properties and explosion scenario are the same as given in Section 2.

Figure 22 shows PPVs and PFs of LPG BLEVE-induced vibrations at different scaled distances and the corresponding empirical fits in the cases of five concrete grades. It can

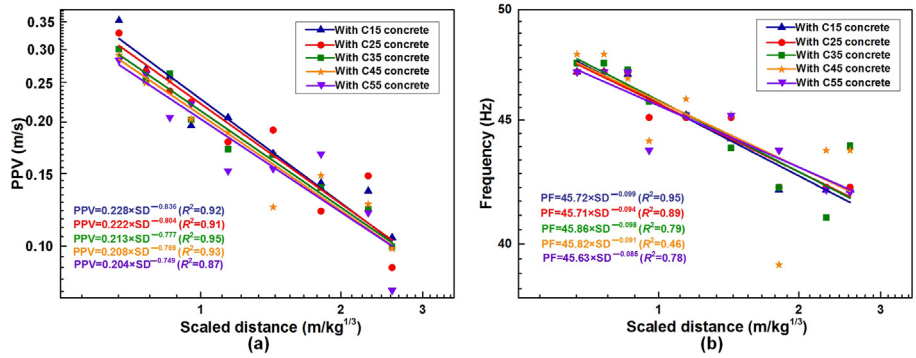

Fig. 22. PPVs and PFs of LPG BLEVE-induced vibrations at different scaled distances and their empirical fits corresponding to the different concrete grades of tunnel linings. (a) PPVs and their best fits, and (b) PFs and their best fits.

be seen that PPVs of blast vibrations at the same scaled distances slightly increase with the decrease of concrete grades. Meanwhile, PFs of blast vibrations of the five cases have very small differences at the same scaled distances, as shown in Fig. 22(b). It can be concluded that varying concrete grades have a negligible influence on the vibration response of surrounding rock mass induced by the internal LPG BLEVE, because the responses of the tunnel and surrounding rock mass mainly depend on the properties of rock mass and its interaction with tunnel structures. However, enhancing the concrete grade of adjacent structures can enhance tunnel safety against LPG BLEVE-induced ground vibrations.

5 Conclusion

This study numerically investigates and compares the vibrations induced by an LPG BLEVE inside an arched tunnel and its equivalent TNT explosion. Multiple factors that influence BLEVE-induced vibrations are investigated to unveil characteristics of BLEVE-induced vibrations. The main conclusions and suggestions are summarized as follows.

(1) The frequency of LPG BLEVE-induced vibrations is lower than that induced by equivalent TNT explosion at the same scaled distance. Compared to the TNT explosion-induced vibration, the LPG BLEVE-induced vibration is less intensive at relatively small scaled distances, but is higher at larger scaled distances (e.g., greater than 1.68 m/kg$^{1/3}$ in this study) because of slower attenuation with distance.
(2) Compared with TNT explosion-induced vibration, the risk of LPG BLEVE-induced vibration (i.e., PPVs combined with PFs) is lower at the relatively small-scaled distances (e.g., less than 1.2 m/kg$^{1/3}$ in this study) but becomes higher at the relatively large-scaled distances.
(3) As compared to concrete grades for lining, other three factors (i.e., cover depth of tunnel, types of rock mass and porosity of rock mass) have more significant influences on the characteristics of LPG BLEVE-induced vibrations. The vibration frequency at the same scaled distance decreases with the increased cover depth. The weaker rock mass and the larger rock porosity lead to higher rock mass vibrations but lower vibration frequencies from the same explosion load. The vibration intensity at the same scaled distances first decreases and then increases with the increased cover depth.
(4) By evaluating PPVs and PFs of LPG BLEVE-induced vibrations, it is found that the cover depth of 30 m that minimizes the combined effects of wave reflection from ground surface and large in-situ stress owing to deep cover leads to the smallest rock mass vibrations among the considered cover depths ranging from 10 to 500 m.

Declaration of competing interest

The authors declare that they have no known competing financial interests or personal relationships that could have appeared to influence the work reported in this paper.

Acknowledgment

The authors acknowledge the financial support from the Australian Research Council (ARC) via the Australian Laureate Fellowship (Grant No. FL180100196).

Appendix A Calculation of BLEVE loads

In the present study, BLEVE loads are obtained using FLACS, which is a CFD software implemented with the Reynolds-averaged Navier-Stokes solver and the BLAST module. The accuracy of FLACS, in simulating the propagation of BLEVE waves, their interaction with structures and the prediction of BLEVE overpressure, has been widely recognized (Li & Hao, 2020). It is worth mentioning that the bursting pressure of LPG tank is first required as the input of BLEVE simulation using FLACS, which is obtained by the energy-based analytical method developed by the authors in the previous study (Li et al., 2022). Several key equations for the energy-based analytical method are given below. Further details can be found in Li et al. (2022).

$$\begin{cases} m_{0\text{liquid}} + m_{0\text{vapor}} = m_{1\text{liquid}} + m_{1\text{vapor}} = m_{2\text{liquid}} + m_{2\text{vapor}} \\ m_{2\text{liquid}} = (1-f)m_{1\text{liquid}} \end{cases} \tag{A1}$$

$$f = 1 - \exp\left(\left(-2.63\frac{C_v}{H_v}(T_c - T_b)\right)\left(1 - \left(\frac{T_c - T_o}{T_c - T_b}\right)^{0.38}\right)\right) \tag{A2}$$

$$\begin{cases} E_1 = E_{s1\text{liquid}}m_{1\text{liquid}} + E_{s1\text{vapor}}m_{1\text{vapor}} \\ E_2 = E_{s2\text{liquid}}m_{2\text{liquid}} + E_{s2\text{vapor}}m_{2\text{vapor}} \end{cases} \tag{A3}$$

where $m_{0\text{–}2\ \text{liquid}}$ and $m_{0\text{–}2\ \text{vapor}}$ are the quality of liquid and vapor at initial state(0), valve release state(1), and final state(2), respectively; f is the fraction of liquid flashing, which is calculated as 96.4% with the liquid initial temperature of 293 K, the critical temperature of 370 K, the boiling temperature of 233 K, the specific heat of 3.2 kJ/(kg·K) at constant pressure of 1.9 MPa (i.e., the set pressure of relief valve), and enthalpy of 351.7 kJ/kg; C_v, H_v, T_c, T_b, and T_o are the specific heat at constant pressure, enthalpy of liquid vaporization, critical temperature of the liquid, boiling temperature of the liquid at atmospheric pressure, and temperature of the liquid at the moment of explosion, respectively; $E_{s1\text{–}2\ \text{liquid}}$ and $E_{s1\text{–}2\ \text{vapor}}$ are the specific internal energy of liquid and vapor at valve release state(1) and final state(2); E_1 and E_2 are the total energy of liquid and

vapor at valve release state(1) and final state(2), respectively.

Based on the E_1 and E_2, the energy released by the bursting of LPG tank to generate BLEVE can be calculated according to Eq. (A4). Then, the finally-generated pressure for the input of BLEVE load simulation can be obtained from Eq. (A5).

$$\Delta U_1 = 0.7\Delta U = 0.7(E_2 - E_1) \tag{A4}$$

$$\Delta U_1 = \left(\frac{P_r}{\gamma - 1}\right) V \left(1 - \left(\frac{P_0}{P_r}\right)^{\frac{\gamma-1}{\gamma}}\right) \tag{A5}$$

Here, ΔU_1 is the energy to generate BLEVE; P_0 is the atmospheric pressure; P_r is the finally-generated pressure; $\gamma$is the ratio of specific heat for propane; V is the volume of the tank.

By inputting the finally-generated overpressure into FLACS, the BLEVE inside tunnel can be simulated by specifying the computational domain, establishing full-size tunnel model, and setting the location and volume of the assumed LPG tank, etc. The tunnel geometry can significantly influence the BLEVE loads and is therefore modelled in detail. The tunnel with the same geometry and size as that built in LS-DYNA is first established in FLACS. The LPG tank with a volume of 20 m^3 as the explosion source is also built inside the tunnel. The specific details of FLACS-simulated BLEVE inside the tunnel can refer to Li et al. (2022). BLEVE loads acting on tunnel walls are finally obtained with the propagation of simulated BLEVE waves and their interaction with tunnel walls. It is worth mentioning that the structures of road tunnel built in FLACS are assumed rigid, which is consistent with the condition of the lining of the actual tunnel constrained by the surrounding rock mass. In addition, it is a general practice to simulate BLEVE with evenly radiated waves by assuming the LPG tanks rupture instantaneously and completely. Therefore, the rupture initiation location on LPG tank (i.e., the explosion centre) has very little influence on the blast waves.

Appendix B TNT equivalence method proposed by Prugh (1991)

The TNT equivalence method proposed by Prugh (1991) is employed in the present study to convert the BLEVE into an equivalent TNT weight. The equations of the TNT equivalence method are given in Eqs. (B1) and (B2). The specific calculation process using the TNT equivalence method and the details of parameter acquisition have been reported in the authors' previous paper (Cheng et al., 2022a) and thus are not repeated again.

$$W_{TNT} = \frac{2.4 \times 10^{-4} P_r V^*}{\gamma - 1} \left(1 - (P_0/P_r)^{(\gamma-1)/\gamma}\right) \tag{B1}$$

$$V^* = V + m_{0liquid}\left(\left(f/D_{2liquid}\right) - \left(1/D_{2vapor}\right)\right) \tag{B2}$$

Here, W_{TNT} is the equivalent TNT weight; V^* is the volume of vapor space; $D_{2liquid}$ and D_{2vapor} are the density of the liquid and saturated vapour at the final state, respectively.

References

Brown, E. T., & Hoek, E. (1978). Trends in relationships between measured in-situ stresses and depth. *International Journal of Rock Mechanics and Mining Sciences & Geomechanics Abstracts, 15*(4), 211–215.

Cao, W., Li, X., Tao, M., & Zhou, Z. (2016). Vibrations induced by high initial stress release during underground excavations. *Tunnelling and Underground Space Technology, 53*, 78–95.

Cheng, R., Chen, W., Hao, H., & Li, J. (2021). A state-of-the-art review of road tunnel subjected to blast loads. *Tunnelling and Underground Space Technology, 112*, 103911.

Cheng, R., Chen, W., Hao, H., & Li, J. (2022a). Dynamic response of road tunnel subjected to internal Boiling Liquid Expansion Vapour Explosion (BLEVE). *Tunnelling and Underground Space Technology, 123*, 104363.

Cheng, R., Chen, W., Li, J., & Hao, H. (2022b). Effects of cover depth and rock type on dynamic response of road tunnels against internal explosions. *International Journal of Applied Mechanics, 14*(7), 2250067.

Domenico, S. N. (1984). Rock lithology and porosity determination from shear and compressional wave velocity. *Geophysics, 49*(8), 1188–1195.

Goel, M. D., Verma, S., Mandal, J., & Panchal, S. (2021). Effect of blast inside tunnel on surrounding soil mass, tunnel lining, and superstructure for varying shapes of tunnels. *Underground Space, 6*(6), 619–635.

Hao, H., Hao, Y., Li, J., & Chen, W. (2016). Review of the current practices in blast-resistant analysis and design of concrete structures. *Advances in Structural Engineering, 19*, 1193–1223.

Hao, H., & Wu, C. (2001). Scaled-distance relationships for chamber blast accidents in underground storage of explosives. *Fragblast, 5*, 57–90.

Hao, H., Wu, Y., Ma, G., & Zhou, Y. X. (2001). Characteristics of surface ground motions induced by blasts in jointed rock mass. *Soil Dynamics and Earthquake Engineering, 21*(2), 85–98.

Hao, Y. F., & Hao, H. (2014). Influence of the concrete DIF model on the numerical predictions of RC wall responses to blast loadings. *Engineering Structures, 73*, 24–38.

Kan, J., Dou, L., Li, X., Cao, J., Bai, J., & Chai, Y. (2022). Study on influencing factors and prediction of peak particle velocity induced by roof pre-split blasting in underground. *Underground Space, 7*(6), 1068–1085.

Lai, H., Wang, S., & Xie, Y. (2016). Study on the fire damage characteristics of the New Qidaoliang Highway Tunnel: Field investigation with computational fluid dynamics (CFD) back analysis. *International Journal of Environmental Research and Public Health, 13*(10), 1014.

Li, J., Hao, H., Chen, W., & Cheng, R. (2022). Calculation of BLEVE energy and overpressures inside a tunnel using analytical and CFD methods. *Tunnelling and Underground Space Technology, 120*, 104263.

Li, J. C., Li, H. B., Ma, G. W., & Zhou, Y. X. (2013). Assessment of underground tunnel stability to adjacent tunnel explosion. *Tunnelling and Underground Space Technology, 35*, 227–234.

Li, J. D., & Hao, H. (2020). Numerical study of medium to large scale BLEVE for blast wave prediction. *Journal of Loss Prevention in the Process Industries, 65*, 104107.

Li, X., Cao, W., Tao, M., Zhou, Z., & Chen, Z. (2016). Influence of unloading disturbance on adjacent tunnels. *International Journal of Rock Mechanics and Mining Sciences, 84*, 10–24.

Liu, K., Li, Q. Y., Wu, C. Q., Li, X. B., & Li, J. (2018). A study of cut blasting for one-step raise excavation based on numerical simulation and field blast tests. *International Journal of Rock Mechanics and Mining Sciences, 109*, 91–104.

Malvar, L. J. (1998). Review of static and dynamic properties of steel reinforcing bars. *ACI Materials Journal, 95*, 609–614.

Mukerji, T., Berryman, J., Mavko, G., & Berge, P. (1995). Differential effective medium modeling of rock elastic moduli with critical porosity constraints. *Geophysical Research Letters, 22*(5), 555–558.

Ministry of Transport of the People's Republic of China (2018). Specifications for design of highway tunnels section 1 Civil engineering. JTG, 3370.1–2018. (in Chinese)

North Atlantic Treaty Organization [NATO], (2010). Manual of NATO safety principles for the storage of military ammunition and explosives AASTP-1.

Paneiro, G., & Rafael, M. (2021). Artificial neural network with a cross-validation approach to blast-induced ground vibration propagation modeling. *Underground Space, 6*(3), 281–289.

Prugh, R. W. (1991). Quantitative evaluation of "Bleve" hazards. *Journal of Fire Protection Engineering, 3*, 9–24.

Tiwari, R., Chakraborty, T., & Matsagar, V. (2016). Dynamic analysis of tunnel in weathered rock subjected to internal blast loading. *Rock Mechanics and Rock Engineering, 49*(11), 4441–4458.

Tiwari, R., Chakraborty, T., & Matsagar, V. (2017). Dynamic analysis of tunnel in soil subjected to internal blast loading. *Geotechnical and Geological Engineering, 35*(4), 1491–1512.

Triviño, L., Mohanty, B., & Milkereit, B. (2012). Seismic waveforms from explosive sources located in boreholes and initiated in different directions. *Journal of Applied Geophysics, 87*, 81–93.

Vernik, L., Bruno, M., & Bovberg, C. (1993). Empirical relations between compressive strength and porosity of siliciclastic rocks. *International Journal of Rock Mechanics and Mining Sciences & Geomechanics Abstracts, 30*(7), 677–680.

Vinod, M., & Khabbaz, H. (2019). Comparison of rectangular and circular bored twin tunnels in weak ground. *Underground Space, 4*(4), 328–339.

Wei, X. Y., Zhao, Z. Y., & Gu, J. (2009). Numerical simulations of rock mass damage induced by underground explosion. *International Journal of Rock Mechanics and Mining Sciences, 46*(7), 1206–1213.

Wu, C., & Hao, H. (2005). Numerical study of characteristics of underground blast induced surface ground motion and their effect on above-ground structures. Part I. Ground motion characteristics. *Soil Dynamics and Earthquake Engineering, 25*(1), 27–38.

Wu, C., Hao, H., Lu, Y., & Zhou, Y. (2003). Characteristics of stress waves recorded in small-scale field blast tests on a layered rock–soil site. *Géotechnique, 53*(6), 587–599.

Wu, C., Lu, Y., & Hao, H. (2004). Numerical prediction of blast-induced stress wave from large-scale underground explosion. *International Journal for Numerical and Analytical Methods in Geomechanics, 28*(1), 93–109.

Wu, C., Lu, Y., Hao, H., Lim, W. K., Zhou, Y., & Seah, C. C. (2003). Characterisation of underground blast-induced ground motions from large-scale field tests. *Shock Waves, 13*(3), 237–252.

Xie, L. X., Lu, W. B., Zhang, Q. B., Jiang, Q. H., Chen, M., & Zhao, J. (2017). Analysis of damage mechanisms and optimization of cut blasting design under high in-situ stresses. *Tunnelling and Underground Space Technology, 66*, 19–33.

Yan, Y., Hou, X., & Fei, H. (2020). Review of predicting the blast-induced ground vibrations to reduce impacts on ambient urban communities. *Journal of Cleaner Production, 260*, 121135.

Yang, H. J. (2006). Deformation characteristic of tunnel surrounding rock under complex conditions. *Journal of Railway Engineering Society, 1*, 57–60, (in Chinese).

Yang, J., Liu, K., Li, X., & Liu, Z. (2020). Stress initialization methods for dynamic numerical simulation of rock mass with high in-situ stress. *Journal of Central South University, 27*(10), 3149–3162.

Zhang, J., Andrus, R. D., & Juang, C. H. (2005). Normalized shear modulus and material damping ratio relationships. *Journal of Geotechnical and Geoenvironmental Engineering, 131*(4), 453–464.

Zhou, Y. (2011). Earthquakes as a rock dynamic problem and their effects on rock engineering structures. *Advances in Rock Dynamics and Applications*, 361–438.

Zhou, Y., Zhao, J., Chong, K., & Seah, C.C., (2002). Dynamic response and tunnel damage from explosion loading. In *Proceeding international symposium on defence construction*, Singapore.

Zhou, Y. X., & Jenssen, A. (2009). Internal separation distances for underground explosives storage in hard rock. *Tunnelling and Underground Space Technology, 24*(2), 119–125.

Zhu, J., Li, Y., Wu, S., Zhang, R., & Ren, L. (2018). Decoupled explosion in an underground opening and dynamic responses of surrounding rock masses and structures and induced ground motions: A FEM-DEM numerical study. *Tunnelling and Underground Space Technology, 82*, 442–454.